Studies in small angle scattering techniques. Experimental methods and examples of their use

Forskningscenter Risø, Roskilde

Publication date:
1980

Document Version
Publisher's PDF, also known as Version of record

Risø-R-396

RISØ

Risø-R-396

Studies in Small Angle Scattering Techniques

Experimental methods and examples of their use

Knud Møllenbach

Risø National Laboratory, DK-4000 Roskilde, Denmark
March 1980

Risø-R-396

STUDIES IN SMALL ANGLE SCATTERING TECHNIQUES
Experimental methods and examples of their use.

Knud Møllenbach

Abstract. Small angle scattering of neutrons, x-rays and γ-rays are found among the spectroscopic methods developed in the recent years. Although these techniques differ from each other in many respects, e.g. radiation sources and technical equipment needed, their power to resolve physical phenomena and areas of application can be discussed in a general scheme. This is the subject of the first part of this report. The rest of the report gives selected examples illustrating the use of specific technical methods. Jahn-Teller driven structural phase transitions in Rare Earth zircons were studied with neutron scattering as well as small angle γ-ray diffraction. The study of neutron scattering from formations of magnetic domains in the Ising ferromagnet $LiTbF_4$ is a second example. Both these examples represent more than experimental test cases since the theoretical interpretations of the data obtained are discussed as well. As a last example the use of small angle scattering methods for the study of molecular biological samples is discussed. In particular the experimental procedures used in connection with scattering from aqueous solutions of proteins and protein complexes are given.

UDC 539.2

March 1980
Risø National Laboratory, DK 4000 Roskilde, Denmark

This report is submitted to the Technical University of Denmark in partial fulfilment of the requirements for obtaining the lic. techn. (Ph.D.) degree.

ISBN 87-550-0580-2
ISSN 0106-2840

Risø Repro 1980

CONTENTS Page

Page

1. INTRODUCTION

The work of a number of experimental physicists throughout the world is dedicated to the development of new spectroscopic instruments capable of measuring larger ranges of momentum and energy transfer to the sample that is the subject of investigation. In general, these efforts aim to widen the field of application of scattering methods, and in particular to make possible more detailed studies of the physical properties of condensed matter.

Instruments designed for the study of elastic scattering (diffraction) of neutrons, X-rays and γ-rays at very small angles are among the most promising for making possible measurements with extreme resolution in momentum transfer. While γ-ray diffraction only gives rather specialized information in crystallography, small-angle scattering of X-rays and neutrons has a rich variety of applications in as different fields of research as solid state physics, chemistry, metallurgy and molecular biology. The key to performing small angle scattering and obtaining the extreme momentum transfer resolution is simply to limit the angular divergence in the radiation beams incident on and scattered from the sample.

This thesis reports on three small angle scattering methods. First, the small angle limit of conventional diffractometers was studied. There are two methods for exceeding this limit. The physical dimensions of the instrument can be extended to give long radiation flight paths. Narrow beam defining slits can then be used to limit the angular divergence of the beams. Alternatively, use can be made of a very narrow beam which is transmitted through a Bragg reflection in a crystal of high perfection. Experiments with instruments in both categories are reported.

Chapters 2 and 3 discuss the basic considerations relating to small angle scattering, and describe the instruments studied,

constructed and used in this work, with special emphasis on the resolving power of the instruments.

As a first example, chapter 4 presents the study of the order parameter near the structural phase transition in three compounds exhibiting a Jahn-Teller transition. γ-ray diffraction was used for the experiments as well as neutron diffraction as a complementary technique.

Chapter 5 describes a study of magnetic domains in the dipolar-coupled Ising ferromagnet $LiTbF_4$. For the experiments use was made of the conventional neutron diffractometer in the small angle limit and a neutron spectrometer employing perfect Si crystals as collimators.

Perhaps the most interesting aspect of small angle scattering is that this technique is becoming an important experimental tool in molecular biological research. As an example chapter 6 discuss the studies of macromolocules in aqueous solutions and gives the result of the considerations and feasibility studies in connection with a proposal for construction of a small angle neutron scattering instrument at the DR 3 reactor of the Risø National Laboratory.

All the construction and testing of instruments and all experiments were performed in the Physics department and at the DR 3 reactor of the Risø National Laboratory except for the studies in molecular biology which were performed in the Biology Department of the Brookhaven National Laboratory, USA.

2. EXPERIMENTAL ASPECTS OF SMALL-ANGLE SCATTERING

Experiments at small scattering angles are performed in order to achieve an extreme resolution in measuring the momentum transfer to the sample that is the subject of investigation.

While it is evident that the resolving power of an experiment depends on the wavelength (or wavevector) of the scattered radiation, the importance of the possible spatial anisotropy of the resolving power is not obvious a priori. It appears that this anisotropy is the key to the understanding of the areas of application of the various instruments, and thus a detailed discussion of the resolving power is the main subject of this chapter.

For completeness, a brief introduction to the vocabulary and most important concepts of small angle scattering is given first. This section is not intended to be a full review, so the reader is referred to the literature for a more extensive discussion (Schmatz et al., 1974 and Bacon, 1975). To emphasize that small angle scattering is a complementary technique, the starting point of the discussion is the general scattering experiment.

2.1. Basic concepts

A general illustration of a scattering experiment is given in fig. 2.1a and b.

Radiation with a wavevector $\bar{k}_1$ and intensity (flux) I_1 is incident on a sample. The radiation scattered from the sample after a momentum transfer $\hbar\bar{\kappa}$ - where $\bar{\kappa}$ is the scattering vector - and possibly an energy transfer, is described by the wavevector $\bar{k}_2$. This radiation is deflected the scattering angle 2θ from the direction of incidence and has the intensity I_2 detected in the solid angle $d\Omega$. The scattering triangle (fig. 2.1b) shows the fulfilment of momentum and energy conservation

$$\hbar\bar{\kappa} = \hbar\bar{k}_1 - \hbar\bar{k}_2 \qquad (2.1)$$

$$E = E_{in} - E_{out}. \qquad (2.2)$$

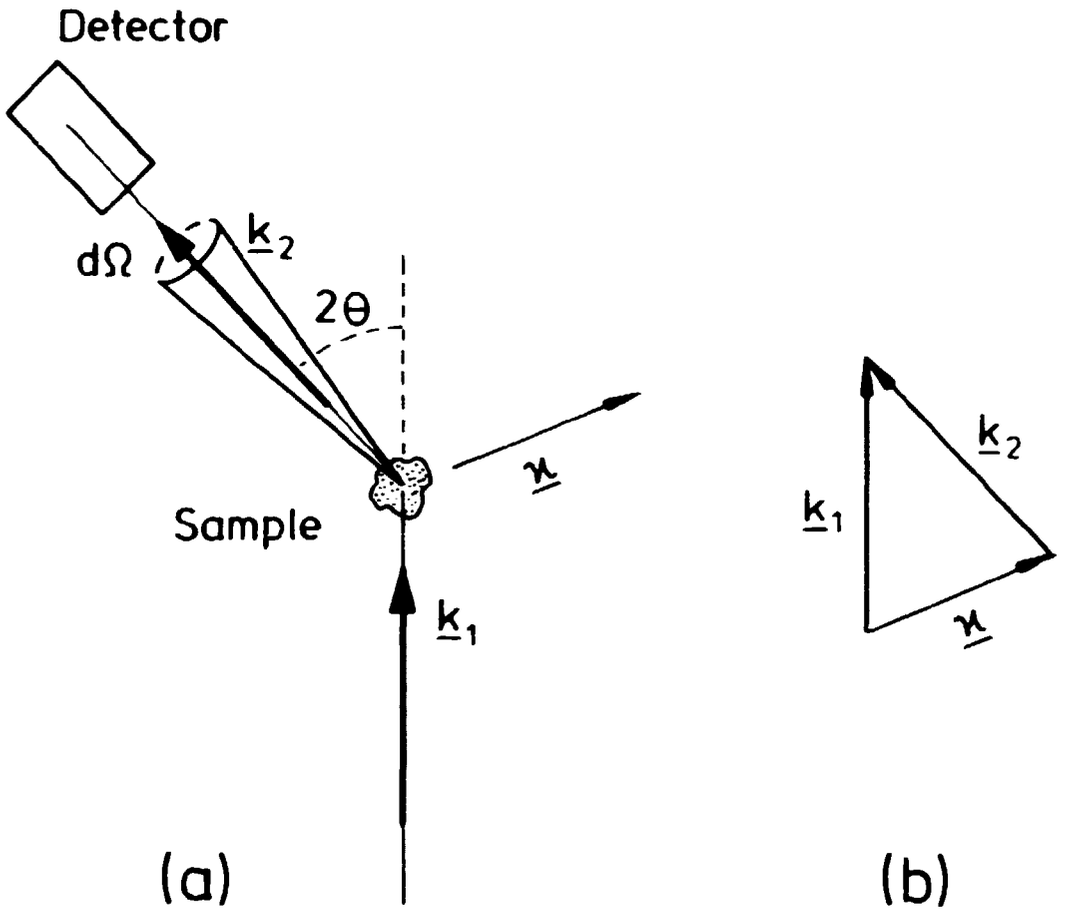

Fig. 2.1. Diagram showing the general scattering experiment (a) and the scattering triangle (b).

The energy relation (2.2) can be rewritten as

$$\hbar\omega = \frac{\hbar^2}{2m} \left(|\bar{k}_1|^2 - |\bar{k}_2|^2\right) \tag{2.3}$$

for particle scattering, and

$$\hbar\omega = \hbar c\left(|\bar{k}_1| - |\bar{k}_2|\right) \tag{2.4}$$

for scattering of electromagnetic radiation.

The interaction between the radiation and the sample is given by the scattering cross-section, defined as the intensity (per

second) of the radiation scattered in the solid angle $d\Omega$ around $\bar{k}_2$, I_2, divided by the incident flux (per m^2 and second), I_1, or

$$\frac{d^2\sigma}{d\Omega dE} = \frac{1}{I_1} \cdot \frac{I_2}{d\Omega dE} \cdot \tag{2.5}$$

This cross-section is commonly known as the double differential cross-section.

The present report is only concerned with elastic scattering, i.e., scattering where E=0. Thus, $|\bar{k}_1| = |\bar{k}_2| = k$ and the scattering triangle shows

$$|\bar{\kappa}| = 2k\sin\theta. \tag{2.6}$$

The scattering cross-section is now the differential cross-section given by

$$\frac{d\sigma}{d\Omega} = \frac{1}{I_1} \frac{I_2}{d\Omega} , \tag{2.7}$$

which is related to the double-differential cross-section by

$$\frac{d\sigma}{d\Omega} = \int \frac{d^2\sigma}{d\Omega dE} dE . \tag{2.8}$$

A very simple example of an elastic scattering cross section is the cross-section for Bragg scattering in a crystal.

$$\frac{d\sigma}{d\Omega} = \text{constant} \cdot \sum_{\tau} \delta(\bar{\kappa}-\bar{\tau}) \tag{2.9}$$

where $\bar{\tau}$ is a reciprocal lattice vector. The delta function in eq. 2.9 gives the Bragg condition

$$|\bar{\tau}| = 2k \sin\theta. \tag{2.10}$$

For small angle scattering, the cross section can be written (Schmatz et al., 1974)

$$\frac{d\sigma}{d\Omega} = \frac{1}{N} \left| \int_V \exp(i\bar{\kappa}\cdot\bar{r}) \sum_{i=1}^{N} b_i \delta(\bar{r}-\bar{r}_i)\, d\bar{r} \right|^2$$

$$= \frac{1}{N} \left| \int_V \exp(i\bar{\kappa}\cdot\bar{r}) \rho(\bar{r}) d\bar{r} \right|^2 \qquad (2.11)$$

where

$$\rho(\bar{r}) = \sum_{i=1}^{N} b_i\, \delta(\bar{r}-\bar{r}_i) \qquad (2.12)$$

is the scattering length density. Here N particles are assumed to be in a volume V, the i'th particle having a position $\bar{r}_i$ and a scattering length b_i. For electromagnetic radiation, N is the number of electrons and b the electron scattering length $r_o = e^2/mc^2$. For nuclear scattering of neutrons, N is the number of nuclei and b the coherent scattering lengths of the nucleus. ρ can in most cases of interest in small angle scattering be treated as a smooth function in space.

Purely elastic scattering is only obtained if the scattering particles are rigidly fixed in space - which they are not. However, the influence of particle motion can be neglected if the squared phase difference of the radiation on passing the particle is small. For diffusive motion, this condition is

$$\hbar D\kappa^2 << E_{in} \qquad (2.13)$$

where D is the self-diffusion constant of the particles. For X-rays and γ-rays, E_{in} is large and the momentary distribution of the scattering particles is obtained. For neutrons with $E_{in} \sim 10^{-3}$ eV, the criterion is fulfilled for $\kappa<0.1\text{Å}^{-1}$, if $D = 10^{-5}$ cm^2 s^{-1}. For critical fluctuations, D is two orders of magnitude larger, and, for neutrons, inelasticity may play a role, see the discussion by Als-Nielsen (1976b). For thermal vibrations, the criterion is

$$\kappa^2 \langle u^2 \rangle << 1 \qquad (2.14)$$

where $\langle u^2 \rangle$ is the mean-square amplitude of vibration of the scattering particles.

For neutron scattering, the inherent background resulting from isotope and spin incoherence is important. The incoherent scattering is nearly isotropic. For a particle with nuclei each having an incoherent cross-section σ_{inc}, one finds in the limit $\kappa \to 0$

$$I_{coh}/I_{inc} = \frac{N \cdot 4\pi b^2}{\sigma_{inc}} . \qquad (2.15)$$

The importance of incoherent scattering depends, of course, on the concentration of incoherent scattering particles in the sample. Incoherent scattering will, in general, always be strong in hydrogen-containing materials since the incoherent cross-section is $\sim$ 80 barn compared with the coherent $\sigma_{coh} = 4\pi b^2 =$ 1.8 barn.

2.2. The resolution function*

It is not possible in any scattering experiment to define $\bar{k}_1$ and $\bar{k}_2$ exactly. Rather, they will be given by some distributions with mean values $\bar{k}_{10}$ and $\bar{k}_{20}$. The probability of observing a scattering process described by a momentum transfer $\bar{\kappa} = \bar{k}_2 - \bar{k}_1$, deviating from $\bar{\kappa}_o = \bar{k}_{20} - \bar{k}_{10}$, and an energy transfer $E = E_2 - E_1$, deviating from $E_o = E_{20} - E_{10}$, will thus be finite, and the probability distribution function $R(\bar{\kappa}-\bar{\kappa}_o, E-E_o)$ is called the resolution function. In the scattering experiment the convolution of this function and the scattering cross-section of the sample is measured. For a qualitative understanding of the resolution function, it is convenient to describe it by its half-value contour, and to imagine this contour to be the probe scanned through $\bar{\kappa}$-E-space - in the sense that all scattering processes with $(\bar{\kappa},E)$ inside the contour contribute uniformly to the scattered intensity, while processes outside the contour make no contribution. As the present report is concentrated on elastic scattering, the discussion is greatly simplified and the resolution function is given as $R = R(\bar{\kappa}-\bar{\kappa}_o)$.

---

*The discussion in this section is based on the ideas and formalism introduced by Bjerrum Møller and Nielsen (1969).

The resolution function is discussed in as simple elements as possible. The calculations are separated into two independent parts, because the components of $\bar{\kappa}-\bar{\kappa}_o$ perpendicular to and in the scattering plane are not correlated. The in-plane (horizontal) part is called $R^h(\bar{\kappa}-\bar{\kappa}_o)$ and the out-of-plane (vertical) part is called $R^v(\bar{\kappa}-\bar{\kappa}_o)$. In most experiments, the calculations can be further separated as the transmission through the system which defines the incoming wavevector, and the transmission through the system which accepts the scattered wavevector, can be considered as independent events.

Gaussian transmission functions are used for beam-defining slits and Soller collimators, and the mosaic distributions of beam-defining and analyzing crystals are assumed to be Gaussian. Finally, deviations from $\tau_o = 2k_o\sin\theta_o$ are assumed to be linear in the deviations of the individual components.

Consider first $R^h(\bar{\kappa}-\bar{\kappa}_o)$. The origin of the contribution to $R^h(\bar{\kappa}-\bar{\kappa}_o)$ from the system defining the incoming wavevector is the distribution of wavevectors $R_1'(\bar{k}_1-\bar{k}_{1o}) = R_1'(\Delta k_{\parallel},\Delta k_{\perp})$. With the assumptions given above, this distribution is in general given by

$$R_1'(\Delta k_{\parallel},\Delta k_{\perp}) = \text{constant} \cdot \exp(Q(\Delta k_{\parallel},\Delta k_{\perp})) \qquad (2.16)$$

where Q is a quadratic form in $\Delta k_{\parallel}$ and $\Delta k_{\perp}$

$$Q(\Delta_{\parallel},\Delta k_{\perp}) = a(\Delta k_{\parallel})^2 + b(\Delta k_{\perp})^2 + 2c\ \Delta k_{\parallel}\cdot\Delta k_{\perp} \qquad (2.17)$$

with

$$a\cdot b - c^2 > 0 \qquad (2.18)$$

Thus, a constant R_1' contour, e.g. the half-value or 1/e value contour, is an ellipse, see fig. 2.2.

The way to find this ellipse is to identify two independent contributions to R_1', each yielding one of two conjugate diameters, $\bar{X}_1$ and $\bar{X}_2$.

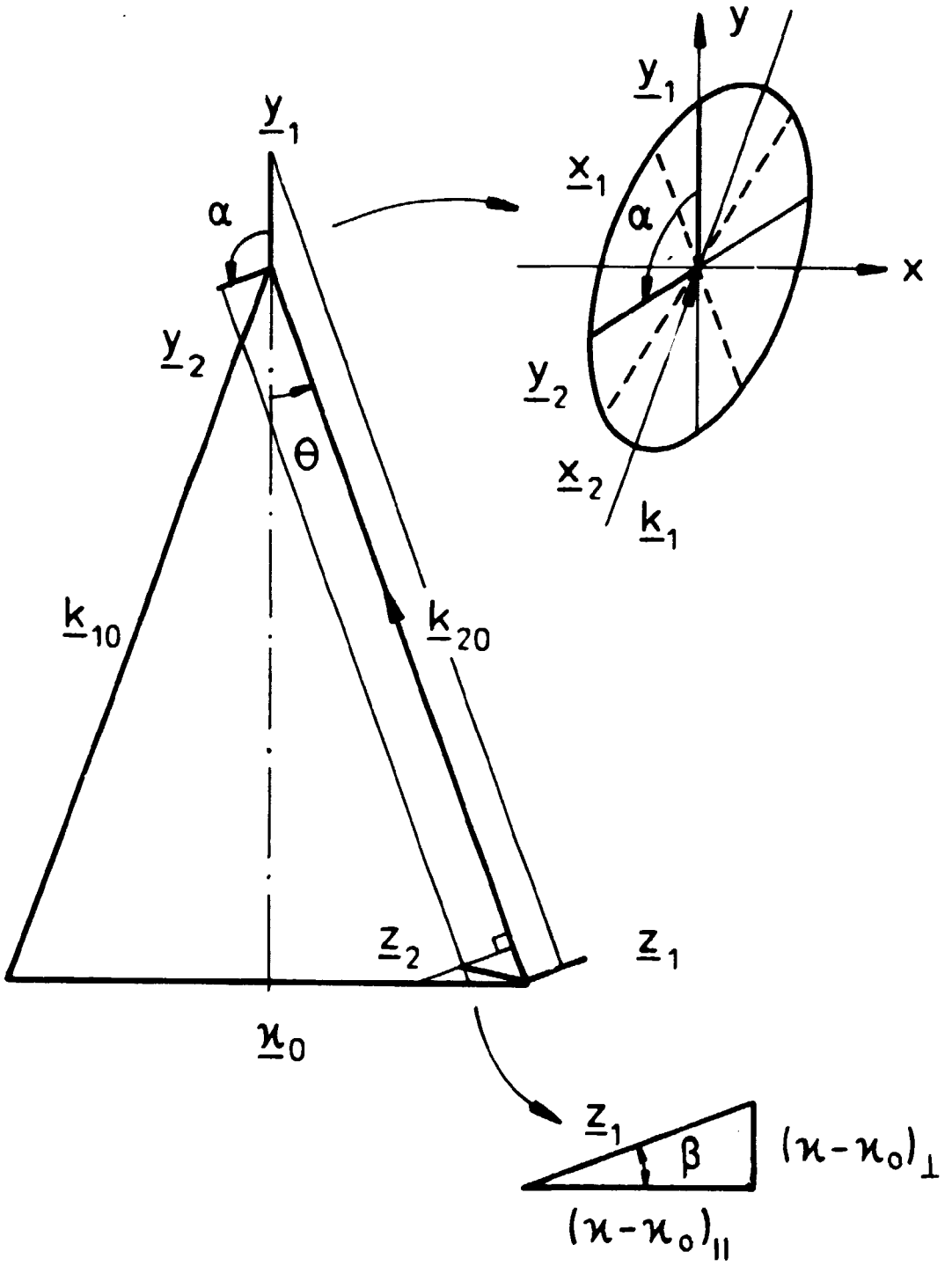

Fig. 2.2. Calculation of the resolution for elastic scattering. The half-contour of "monochromatic" neutrons is an ellipse given by the set $(\bar{X}_1, \bar{X}_2)$ or $(\bar{Y}_1, \bar{Y}_2)$ of conjugate diameters. In the elastic scattering process the set $(\bar{Y}_1, \bar{Y}_2)$ is transformed to the set $(\bar{Z}_1, \bar{Z}_2)$ giving the final resolution ellipse.

The R_1' contour ellipse is to be transformed to a contour of the distribution $R_1(\bar{\kappa}-\bar{\kappa}_o)$ around the endpoint of $\bar{\kappa}_o$. In the linear approximation mentioned above this transformation will be given as follows: A vector $\bar{k}_1-\bar{k}_{1o}$ is transformed to a vector $\bar{\kappa}-\bar{\kappa}_o$ by

$$(\bar{\kappa}-\bar{\kappa}_o)_{\shortparallel} = |\bar{k}_1-\bar{k}_{1o}| \cdot \{2\cos\alpha'\cdot\sin\theta - \sin\alpha'\cdot\cos\theta\}$$

$$(\bar{\kappa}-\bar{\kappa}_o)_{\perp} = |\bar{k}_1-\bar{k}_{1o}| \cdot \{\sin\theta\cdot\sin\alpha'\} \qquad (2.19)$$

where α' is the angle between $\bar{k}_{1o}$ and $\bar{k}_1-\bar{k}_{1o}$,

It is seen that

$$\cot\beta = \frac{(\bar{\kappa}-\bar{\kappa}_o)_{\shortparallel}}{(\bar{\kappa}-\bar{\kappa}_o)_{\perp}} = 2\cot\alpha' - \cot\theta. \qquad (2.20)$$

Because of this equation it is convenient to have the contour ellipse of R_1' given by a set of conjugate diameters $\bar{Y}_1$ and $\bar{Y}_2$, where the angle between $\bar{Y}_1$ and $\bar{k}_{1o}$ is θ, or in other words $\bar{Y}_1$ is perpendicular to $\bar{\kappa}_o$.

The formulas relating the original conjugate diameters $\bar{X}_1$ and $\bar{X}_2$ and $\bar{Y}_1$ and $\bar{Y}_2$ are given in appendix A.

The conjugate diameters in the contour ellipse of $R_1(\bar{\kappa}-\bar{\kappa}_o)$ resulting from the transformation of $\bar{Y}_1$ and $\bar{Y}_2$ through eq. 2.20 are called $\bar{Z}_1$ and $\bar{Z}_2$. Note that $\bar{Z}_1$ is perpendicular to $\bar{k}_{20}$.

It is then simple to reach the final contour ellipse of $R^h(\bar{\kappa}-\bar{k}_o)$. Independent contributions, i.e., contributions confined to a line in the scattering plane, are identified and included one by one. Each contribution will elongate the R_1 contour along one line as follows: The contribution to be included is given by $\bar{Z}_1''$. To describe the R_1 contour, a new set of conjugate diameters $\bar{Z}_1'$, $\bar{Z}_2'$ is chosen with $\bar{Z}_1' \parallel \bar{Z}_1''$. $\bar{Z}_1''$ is then included by setting

$$|Z_1'|_{incl} = (|Z_1'|^2 + |Z_1''|^2)^{\frac{1}{2}}. \qquad (2.21)$$

When all contributions have been included by this procedure the resolution function $R^h(\bar{\kappa}-\bar{\kappa}_o)$ is calculated.

Often the collimation between the sample and the detector is the only important contribution to be included. For this contribution $\bar{Z}_1''$ is perpendicular to $\bar{k}_{20}$, and the convenience of choosing $\bar{Y}_1$ and $\bar{Z}_1$, as described above, is clear. It is further seen that the physics behind the transformation (2.19) is to assume infinitesimal collimation between the sample and the detector.

Finally, with respect to the vertical resolution the calculation is very simple using the assumptions given above. If the transmission through the $\bar{k}_1$ defining system and the $\bar{k}_2$ accepting system is given by Gaussian functions with widths X_3 and Z_3, respectively, then $R^v(\bar{\kappa}-\bar{\kappa}_o)$ is a Gaussian function with width $(X_3^2+Z_3^2)^{\frac{1}{2}}$.

2.3. An example: The neutron diffractometer

For the sake of generality, the preceding section was kept in very formal and abstract language, which enables the theory to be used for a variety of instruments of very different mechanical construction. To illustrate the use of the formalism, it will be applied to a well-known instrument: the neutron diffractometer. A sketch of the neutron diffractometer is shown in fig. 2.3.

A neutron beam with a Maxwellian energy-distribution emerges from a beam hole in the reactor. A narrow energy band is selected from this beam by a monochromator crystal and two Soller collimators. The monochromatic beam is incident on a sample and the diffracted radiation is passed through a collimator and detected. The detector and sample can be rotated independently. Thus this instrument can measure the differential cross-section in a range limited by the incident wavevector and the maximum and minimum accessible scattering angle. Typical values are

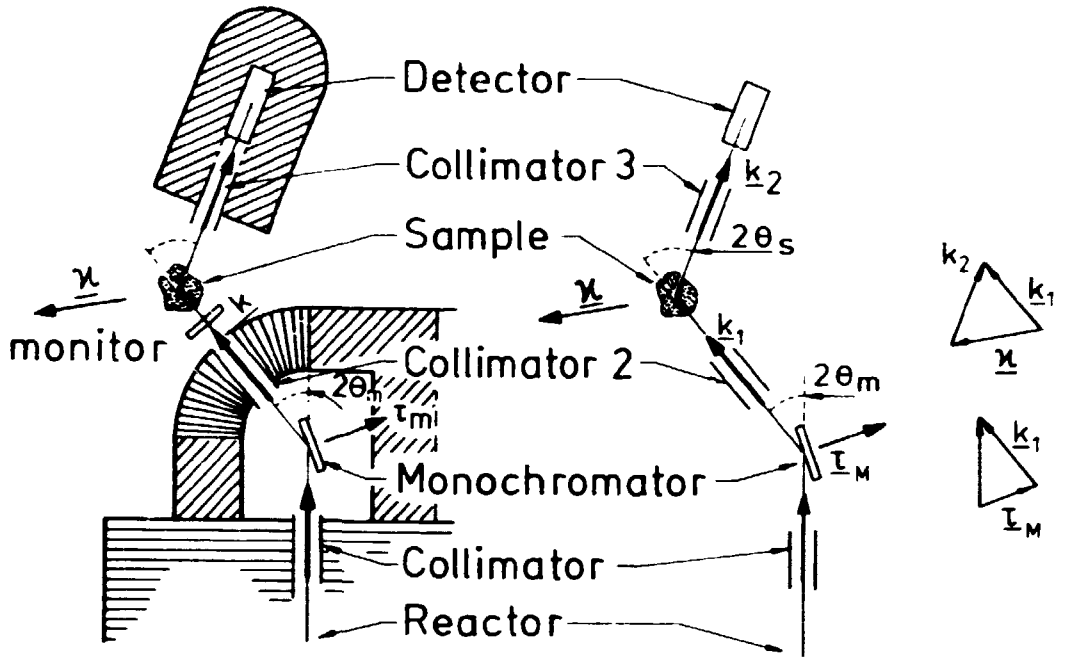

Fig. 2.3. The neutron diffractometer.

$k_1 \sim 2\text{Å}^{-1}$, $\theta_{max} \sim 55^o$ and $\theta_{min} \sim .4^o$, and thus $3.3\ \text{Å}^{-1} > \kappa > .02\ \text{Å}^{-1}$.

$\bar{X}_1$ and $\bar{X}_2$ are easily recognized. $\bar{X}_1$ describes the distribution of wavevectors transmitted through the monochromator system, assuming the monochromator crystal to be perfect. $\bar{X}_2$ describes the smearing of the $\bar{X}_1$ distribution due to the finite mosaic width of the monochromator crystal. Figure 2.4 illustrates these contributions - the scattering diagram in the figure is the scattering triangle of the monochromator crystal.

$\bar{X}_1$ and $\bar{X}_2$ were calculated by Bjerrum Møller & Nielsen (1969) as

$$|\bar{X}_1| = \frac{k}{\sin u_1} \frac{\sigma_o \sigma_1}{(\sigma_o^2+\sigma_1^2)^{\frac{1}{2}}}$$

$$\alpha_1' = \theta_m$$

$$|\bar{X}_2| = \frac{k}{\sin u_2} \frac{2\sigma_1^2}{\sigma_o^2+\sigma_1^2} \left[\frac{4}{\sigma_o^2+\sigma_1^2} + \frac{1}{\eta_m^2}\right]^{-\frac{1}{2}} \qquad (2.22)$$

$$\operatorname{tg} \alpha_2' = \operatorname{tg}\theta_m \cdot \frac{2\sigma_1^2}{\sigma_1^2-\sigma_o^2} \quad , \quad o < \alpha_2' \leq \pi$$

where σ_o is the width of the collimation between the reactor and the monochromator crystal, σ_1 between the monochromator crystal and the sample, and η_m is the mosaic width of the monochromator crystal.

After the sample, as mentioned earlier, the collimation gives a contribution to the resolution perpendicular to the scattered wavevector. One other contribution may be important, namely the mosaic distribution of a crystalline sample. This contribution is along a direction perpendicular to the momentum transfer vector.

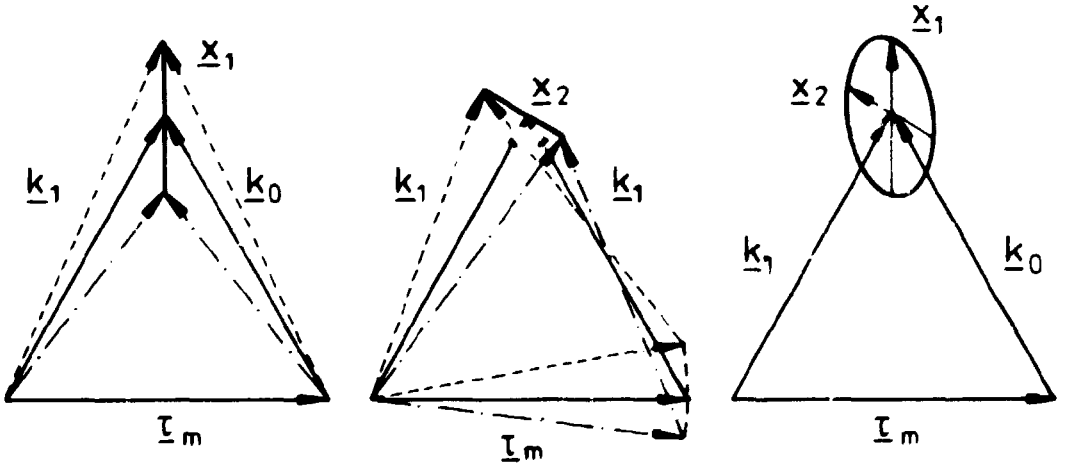

Fig. 2.4. Identification of the two independent contributions yielding the set $(\bar{X}_1, \bar{X}_2)$ of conjugate diameter. $\bar{X}_1$ describes the distribution of wavevectors transmitted through the monochromator system, assuming the monochromator crystal to be perfect. $\bar{X}_2$ describes the smearing of $\bar{X}_1$ due to the finite mosaic width of the monochromator crystal.

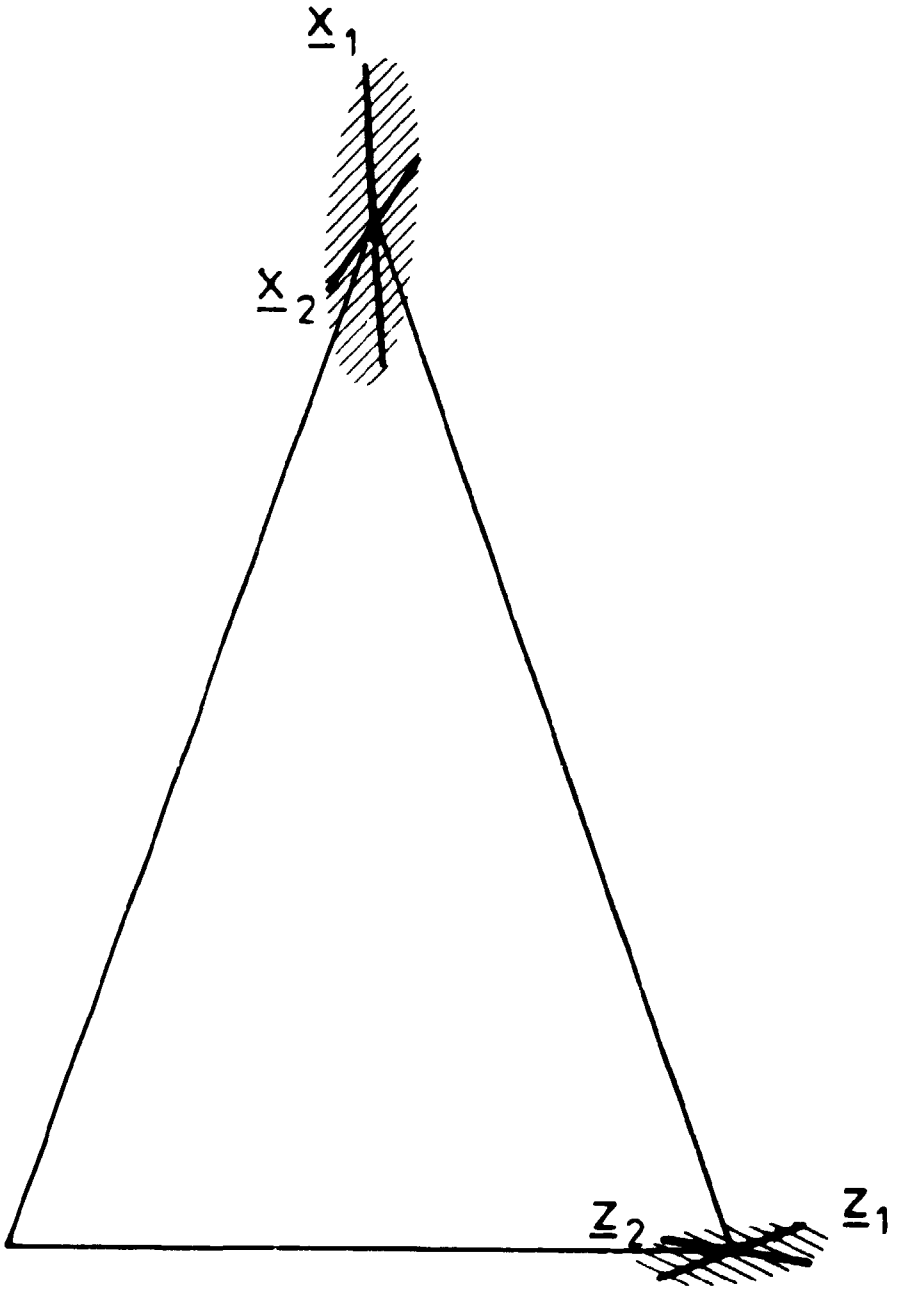

Fig. 2.5. Computer calculation of the resolution function. The scattering triangle is drawn to scale 1/25. The following parameter values were used: $k = 2.5$ Å^{-1}, $\kappa = 1.7$ Å^{-1}, $\sigma_o = 30'$, $\sigma_1 = \sigma_2 = 15'$ and $\eta_m = 20'$.

Hereby all elements ready to insert in the scheme set up in the preceding section are identified. As indicated, this is a task for an electronic calculator, and an output is seen fig. 2.5 where the typical values $k = 2.5\ \text{Å}^{-1}$, $\kappa = 1.7\ \text{Å}^{-1}$, $\sigma_o = 30'$, $\sigma_1 = \sigma_2 = 15'$ and $\eta_m = 20'$ are used.

2.4. The resolution function in the small angle limit

In the limit of small scattering angles, the transformation formulas in section 2.2 are very simple.

Let the vectors $\bar{Y}_1$ and $\bar{Y}_2$ be given. The lengths of the vectors are called Y_1 and Y_2, and the angle between them α. $\bar{Z}_1$ - the transformation of $\bar{Y}_1$ - is, for $\theta \ll 1$, given by

$$Z_{1,\parallel} = Y_1 \cdot \theta$$

$$Z_{1,\perp} = Y_1 \cdot \theta^2 \qquad (2.23)$$

and $Z_1 = |\bar{Z}_1| = Y_1 \cdot \theta$ and $\beta_1 = \theta$.

$\bar{Z}_2$ - the transformation of $\bar{Y}_2$ - is given by

$$Z_{2,\parallel} = - Y_2 \cdot \sin\alpha$$

$$Z_{2,\perp} = Y_2 \cdot \sin\alpha \cdot \theta \qquad (2.24)$$

or $Z_2 = |\bar{Z}_2| = Y_2 \cdot \sin\alpha$ and $\beta_2 = \pi - \theta$.

Inclusion of the collimation after the sample changes Z_1 to

$$Z_1 = (Y_1^2 \cdot \theta^2 + k^2 \cdot \sigma_2^2)^{\frac{1}{2}} \qquad (2.25)$$

and the width of the resolution ellipse parallel and perpendicular to $\bar{\kappa}_o$ are

$$R_{\parallel} = 2\left(\frac{Z_1^2 \cdot Z_2^2}{Z_1^2+Z_2^2}\right)^{\frac{1}{2}}$$

$$R_{\perp} = 2\left(\frac{Z_1^2 \cdot Z_2^2}{Z_1^2+Z_2^2}\right)^{\frac{1}{2}} \cdot \theta \ . \qquad (2.26)$$

It is seen that the resolution ellipse has a pathological elongated shape. In the perpendicular direction, the ellipse is very narrow and confined to the parallel direction. Thus, if an instrument is designed to give a narrow resolution in the parallel direction of $\bar{\kappa}_o$, the resolution in the perpendicular direction is automatically extremely narrow, while the reverse is not necessarily true. The discussion of the instruments in the next chapter is based on the simple results of this section.

2.5. The small angle limit of the neutron diffractometer

The neutron diffractometer is at its small angle limit when $|\bar{\kappa}| < .1$ Å^{-1}. This limit is easiest to reach with low energy neutrons (cold neutrons), say, 5 meV neutrons. The wavelength of these are approximately 4 Å. The practical lower width limit of Soller collimators is $\sigma = 10'$.

For $\sigma_o \gg \sigma_1 \sim \sigma_2 \sim \eta_m$, the formulas of sec. 2.3 are reduced to:

$$X_{1\parallel} = -k \cdot \sigma_1 \qquad X_{2\parallel} \sim 0$$

$$X_{1\perp} = k \cdot \sigma_1 \cdot \cot\theta_m \qquad X_{2\perp} = -k \cdot \eta_m \cdot \cot\theta_m \qquad (2.27)$$

which are the components of $\bar{X}_1$ and $\bar{X}_2$ parallel and perpendicular to $\bar{\kappa}$. The transformation given in appendix A yields

$$Y_1 = k \cdot \eta_m \cdot \cot\theta_m$$

$$Y_2 = k \cdot \sigma_1 / \sin\theta_m \qquad \tan\alpha = -\cot\theta_m \qquad (2.28)$$

Then it is easy to find

$$Z_1 = (Y_1^2 \cdot \theta^2 + k^2 \cdot \sigma_2^2)^{\frac{1}{2}} \simeq k \cdot \sigma_1$$
$$Z_2 = k \cdot \sigma_1 \cdot \cot\theta_m \tag{2.29}$$

and hence

$$R_\perp = 2 \cdot \kappa \cdot \sigma_1 \cdot \cos\theta_m$$
$$R_\parallel = 2 \cdot k \cdot \sigma_1 \cdot \cos\theta_m \tag{2.30}$$

For 5 meV neutrons and a graphite monochromator,

$$\cos\theta_m \simeq \frac{\sqrt{2}}{2} \tag{2.31}$$

and

$$R_\perp \simeq \sqrt{2}\ \kappa \cdot \sigma_1 = 4 \cdot 10^{-3} \cdot \kappa$$
$$R_\parallel \simeq \sqrt{2}\ k \cdot \sigma_1 = 6 \cdot 10^{-3}\ \text{Å}^{-1} \tag{2.32}$$

This is the resolution of the neutron diffractometer at the small angle limit. The smallest accessible κ is

$$\kappa_{min} \simeq 2 \cdot 2.6 \cdot \sigma_1 \cdot k \simeq .02\text{Å}^{-1} \tag{2.33}$$

(at $\theta \simeq 2.6 \cdot \sigma_1$, the primary beam is attenuated 1000 times).

Operating the neutron diffractometer at this limit has proved to be useful for studying critical phenomena near the (ooo) "Bragg-point" (Als-Nielsen, 1976a). In the present work the diffractometer was used to study neutron scattering from magnetic domains in a uniaxial ferromagnet, see chapter 5.

3. SMALL ANGLE SCATTERING INSTRUMENTS

The calculations in chapter 2 showed that a condition necessary for obtaining a high resolution in a small angle scattering experiment is the use of instruments with very narrow collimations of incident and scattered radiation.

This chapter describes the principles of some instruments fulfilling these requirements. The resolution function and areas of application of the instruments are discussed. Throughout the chapter the notation from chapter 2 is used without special comments.

3.1. The double-crystal spectrometer - the DCS

A high-resolution, small angle instrument can be constructed as a slightly modified neutron triple-axis spectrometer (TAS), but both X-rays and neutrons can be used as radiation. A sketch of the DCS is seen in fig. 3.1. Radiation from a beam port is passed through a collimator and is incident on a perfect crystal. For one given radiation energy, only a beam with a width equal to the mosaic width of the crystal is transmitted in a direction dependent on the energy as determined by the Bragg equation. If a "white" beam emerges from the beam port, then a "fan" of radiation will be transmitted through the collimator and crystal, but in the fan there is a one-to-one relation between the direction of the radiation and its energy. The width of the fan is given by the first collimator. Thus the collimator and the crystal act as an energy band-pass filter and the crystal as an effective, very narrow collimator. In the case of a monochromatic radiation source, no energy filtering is needed and the collimator in front of the crystal can be omitted.

After passing the crystal, the radiation is incident on the sample and before the scattered radiation is detected it is Bragg-reflected from a second perfect crystal acting as a very narrow collimator.

When operating the instrument, the first crystal is kept fixed. Rotation of the sample (scan in ω) is equal to scanning perpendicular to the momentum transfer vector, and rotation of the second crystal equals a scan in the length of the momentum transfer vector (scan in 2θ). As mentioned, the DCS can be constructed as a small modification of a TAS. The two perfect crystals simply replace the monochromator and analyser crystals,

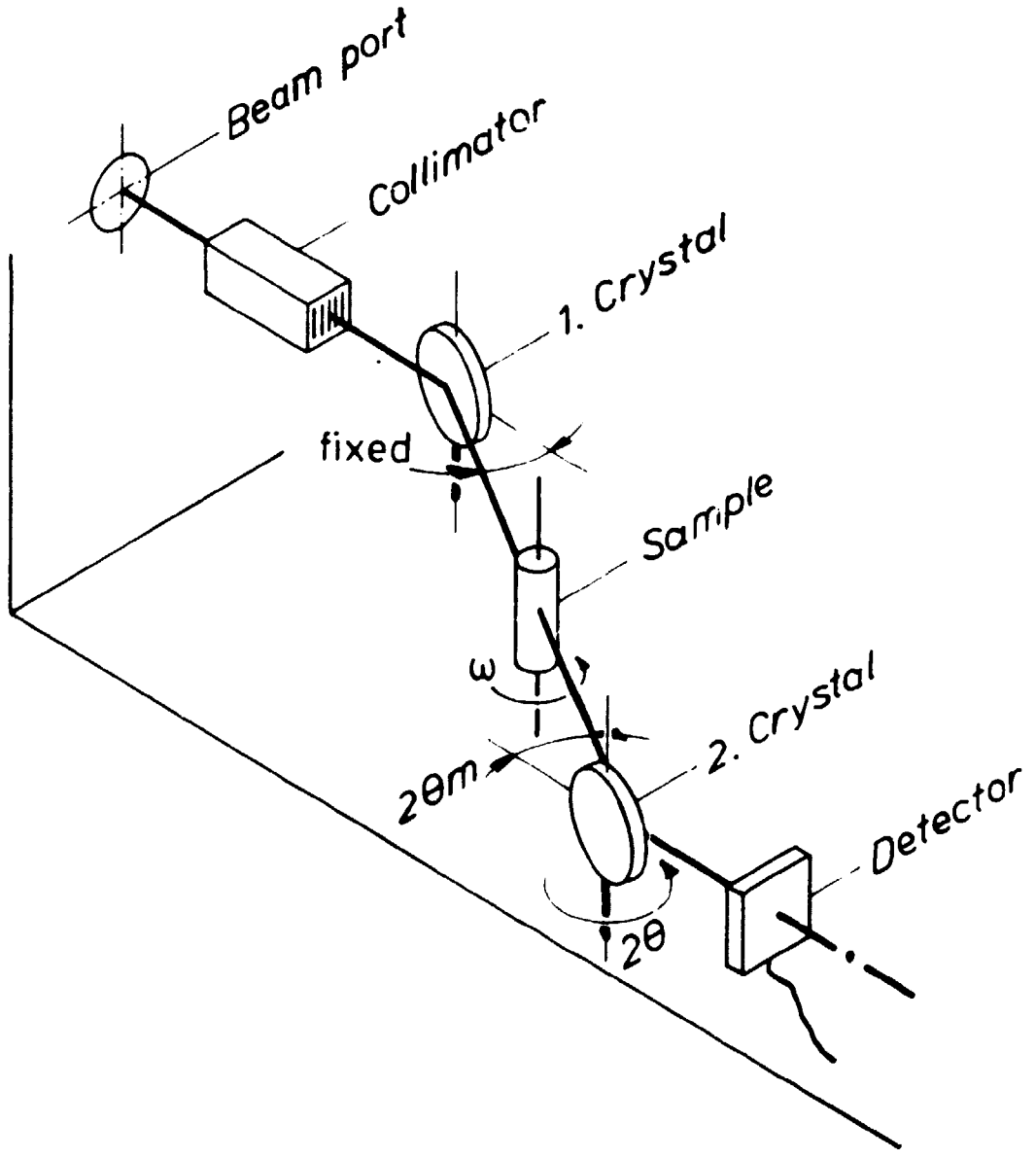

Fig. 3.1. A sketch of the Double Crystal Spectrometer - the DCS.

but a very precise rotation is required of the second crystal, with typical precision one arc second.

The crystals best suited for a DCS are Ge and Si crystals as they can be obtained commercially with a mosaic width of a few arc seconds, typical 10-25".

The resolution of the DCS:
Consider first a monochromatic radiation source. $\bar{Y}_1$ degenerates to the zero-vector and $\bar{Y}_2$ is a vector perpendicular to $\bar{k}_{10}$ with a length $k \cdot \eta_1$, where η_1 is the mosaic-width of the first crystal. The contribution $\bar{Z}_1''$ is perpendicular to $\bar{k}_{20}$ and with a length $k \cdot \eta_2$ where η_2 is the mosaic-width of the second crystal. If $\eta_1 = \eta_2 = \eta$, then the resolution ellipse has its major axis along the momentum transfer vector and $R_{\parallel} = k \cdot \eta$ and $R_{\perp} = k \cdot \eta \cdot \theta$. Typical values are $k = 1.55 \text{Å}^{-1}$, $\eta = 10' \sim 5 \cdot 10^{-5}$ rad, $\theta_{min} \sim 2{,}6 \cdot \eta$, and hence $R_{\parallel} \sim 10^{-4}$ Å^{-1} and $R_{\perp,min} \sim 5 \cdot 10^{-9}$ Å^{-1}.

A characteristic line emitted by a rotating-anode X-ray generator is an example of a monochromatic source. It should be noted that the X-ray DCS is also a high resolution instrument at larger scattering angles, as discussed by Als-Nielsen et al (1977).

If the radiation source is "white", the resolution ellipse given above is smeared. Assume $\eta = 0$, then the monochromatic resolution function is a delta-function and the "white" beam resolution function is a vector $\bar{Z}_4$ with length $|\bar{Z}_4| = k \cdot \cot\theta_c \cdot \sigma_o \cdot \theta$, and the angle between $\bar{Z}_4$ and $\bar{\kappa}$, γ, is given by $\tan\gamma = \frac{1}{2} \tan\theta_c$, where θ_c is the mean scattering angle for the perfect crystals, and σ_o is the width of the collimators in front of the first crystal, see fig. 3.2.

It is seen that the effect of the "white" beam can be included in the same way as contributions from the radiation acceptance system, see eq. 2.21.

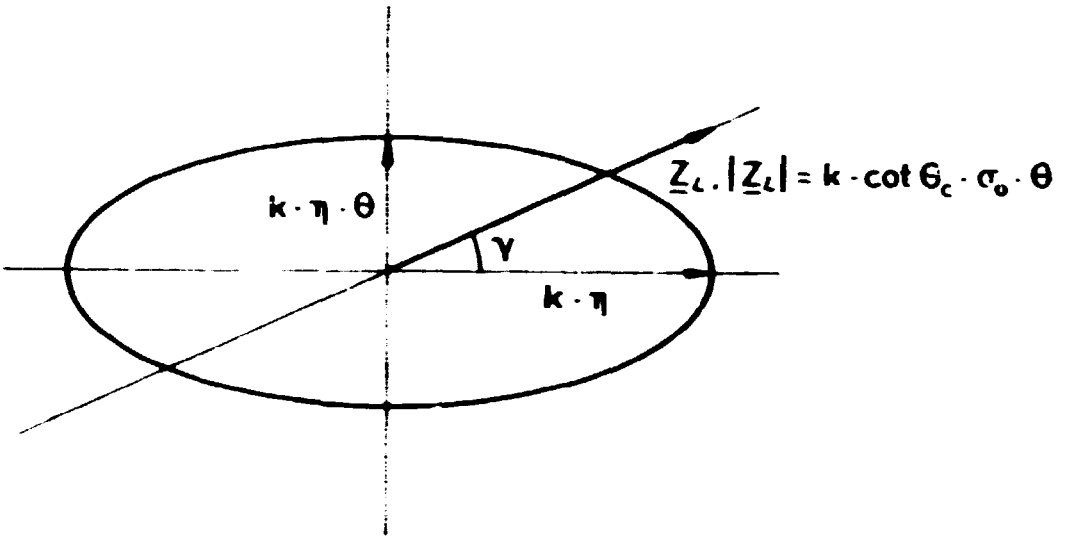

Fig. 3.2. The "white" beam resolution function is given by a smearing of the monochromatic resolution function.

$|\bar{Z}_4|$ and R_* can be compared to determine when the effect is important. Because $\cot\theta_c \sim 1$, it is seen that the criterion for neglecting $\bar{Z}_4$ is $\sigma_o \cdot \theta \ll \eta$. For $\sigma_o = 2^o = .03$ rad, then the criterion is $\theta < 30 \cdot \eta$ thus the appreciable band-width is acceptable.

The neutron beam from a reactor and the X-ray beam from a synchrotron are examples of "white" radiation sources. The σ_o-collimation obtained from the construction of a neutron beam port in a reactor has typically a width as given above. The collimation of the synchrotron beam is much finer, due to the fact that the radiation is observed in the laboratory frame rather than in the moving electron reference frame, and the typical value is $\sigma_o \sim 10''$.

The X-ray DCS has only recently been constructed (Als-Nielsen et al 1977) and so far only used at large scattering angles. The neutron DCS has been used for several studies measuring, e.g., the forward neutron scattering length in iron and void distributions in metals (Annual Report, ORNL 1977). This report

presents another example in chapter 5 - a study of scattering from magnetic domains in a uniaxial ferromagnet.

3.2. The γ-diffractometer - the GAD

The only possibility of obtaining a narrow collimation other than that described in the preceding section, is to extend the linear dimensions of the instrument. A very simple example of this kind of instrument is the GAD (Schneider, 1974a and Møllenbach, 1975). A sketch is seen in fig. 3.3.

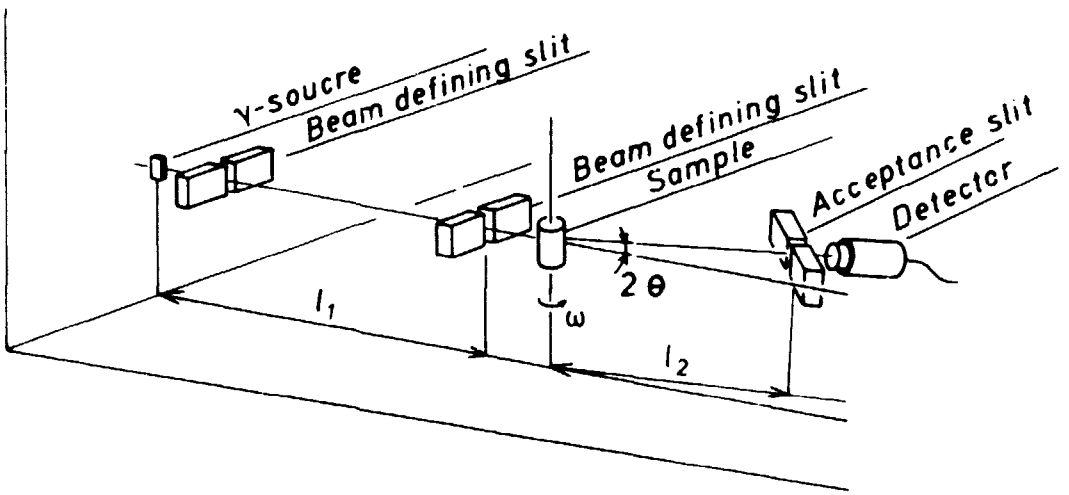

Fig. 3.3. A sketch of the γ-diffractometer - the GAD.

Monochromatic γ-radiation from an intense source is passed through a long single slit collimator. The length, ℓ_1, is typically 3 m and the minimum slit width 0.2 mm, and thus σ_1 = 14". The γ-radiation is incident on a sample and the scattered radiation is passed through a slit before detection. The length, ℓ_2, from the sample to the detector slit is typically 1.5 m, and the slit width 4 mm. Thus $\sigma_2 >> \sigma_1$.

The resolution of the instrument is calculated in exactly the same way as in the monochromatic DCS case and

$$R_{\parallel} = k \cdot \sigma_1$$

$$R_{\perp} = \kappa \cdot \sigma_1 . \qquad (3.1)$$

The energy of the γ-rays is much higher than that of X-rays and neutrons, and for the 412 keV line in 198-Au one finds k = 209 $Å^{-1}$, yielding

$$R_{\parallel} = .015\ Å^{-1}$$

$$R_{\perp} = \kappa \cdot 6.7 \cdot 10^{-5} \qquad (3.2)$$

The resolution appears poor in the parallel direction but extremely fine in the perpendicular direction. This limits the use of the instrument to rather specialized tasks. The instrument can only use single crystals as samples and only measure properties with a κ-dependence perpendicular to a reciprocal lattice vector τ.

An interesting property of this kind is the mosaic-distribution in a crystal. As extinction is negligible in a γ-diffraction experiment (Schneider 1975b), the mosaic-distribution can be measured absolutely with high precision. The GAD can also give precise measurements of shear mode strains and an example of this is given in chapter 4, where a study of some structural phase transitions is presented.

3.3. The neutron small angle scattering instrument - the SAS

The most powerful small angle scattering instrument to be described here is the neutron long flight path instrument. This is another example of an instrument where narrow collimation has been obtained by extension of the linear dimensions of the instrument.

A sketch of the instrument is seen in fig. 3.4. Cold neutrons (E < 5 meV) emerge from a beam port in a reactor and are mono-

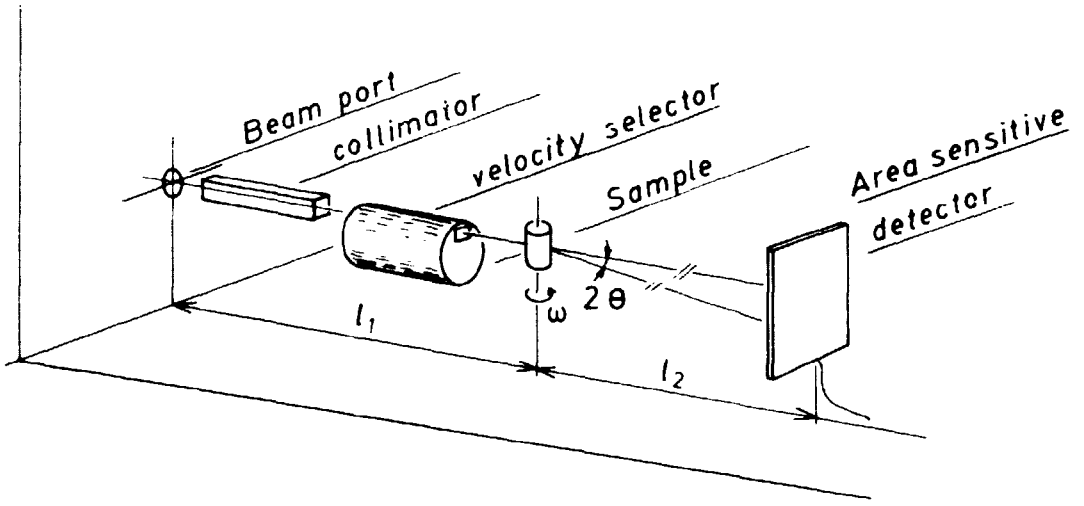

Fig. 3.4. A sketch of the neutron small angle scattering instrument - the SAS.

chromatized by a velocity selector in connection with a fine collimator before hitting the sample. The velocity selector is a rotating drum with neutron absorbing plates at a small angle with respect to the axis of rotation, which coincides with the incident beam direction, see fig. 3.5. Only neutrons within a certain velocity interval, or equivalently a certain wavelength interval, avoid hitting the plates. The width and mean value of the wavelength interval can be varied by changing the rotation speed and/or the angle between the beam and the rotation axis.

The scattered radiation is detected in an area-sensitive detector. The collimation between sample and detector is given by the distance between these two, the size of the sample or a sample-defining mask, and the size of the detector element. Typical values for the dimensions of the instrument will be given after the calculation of the resolution function.

The resolution of the SAS:
The transmission function of the collimator before the velocity selector is as usual a Gaussian with a width σ_2. The transmission function of the velocity selector is found in the following way: Consider the neutron wavevector in a reference frame

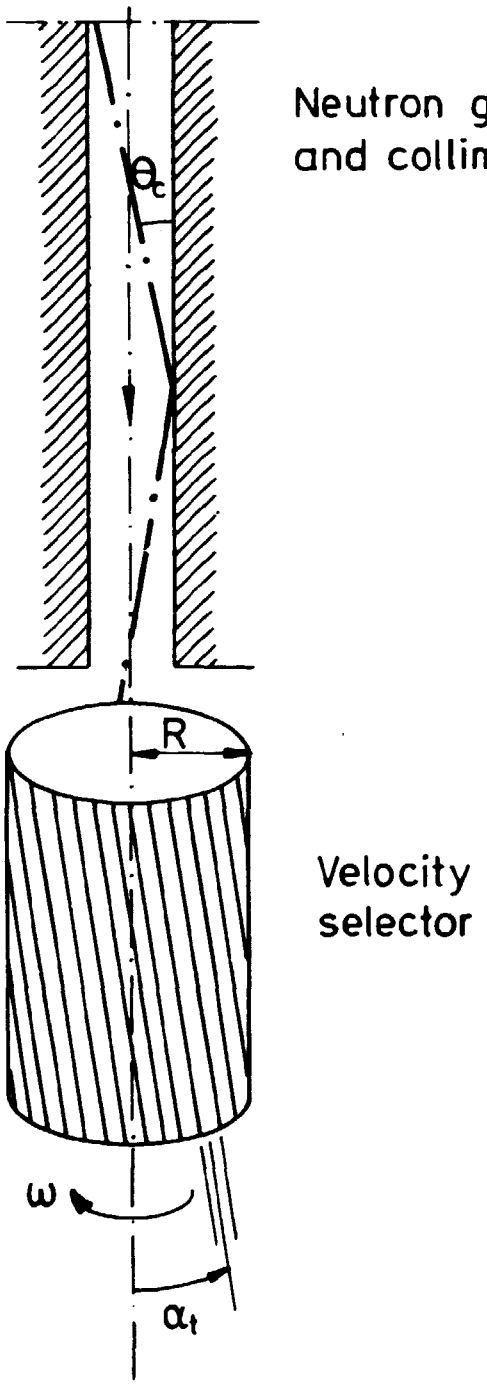

Fig. 3.5. A sketch of the neutron guide tube and the velocity selector. A velocity selector at Risø has the dimensions R = 83 mm, and a length of 400 mm.

moving with the same velocity as the plates in the velocity selector. In this frame the slit is stationary and acts as ordinary collimator plates, the collimator having a width σ_1. Thus the probability of transmission through collimator and velocity selector is

$$P = P_1(\varepsilon) \cdot P_2(y) \tag{3.3}$$

where

$$P_1(\varepsilon) = \exp\left(-\frac{\varepsilon^2}{\sigma_1^2}\right), \quad \varepsilon = \frac{\kappa'}{k_o} \cdot \frac{\Delta k_\parallel}{k_o} + \frac{\Delta k_\perp}{k_o} \equiv \frac{\kappa'}{k_o} \cdot x + y \tag{3.4}$$

and

$$P_2 = \exp\left(-\frac{y^2}{\sigma_2^2}\right) \qquad y \equiv \frac{\Delta k_\perp}{k_o} . \tag{3.5}$$

The definitions of the parameters are obvious from fig. 3.6. κ' is given by

$$\kappa' = \frac{m}{\hbar} \cdot v = \frac{m}{\hbar} \cdot 2\pi R \cdot \nu . \tag{3.6}$$

The optimal k equal to k_{opt} is given by

$$k_{opt} = \frac{m}{\hbar} \cdot v_o = \frac{m}{\hbar} 2\pi \cdot R \cdot \nu \cdot \frac{1}{\alpha_t} \tag{3.7}$$

where R and α_t are defined in fig. 3.5 and ν is the rotation frequency of the velocity selector.

Now the coordinate set (x,y) is transformed to a set (x_1,x_2), for which

$$P = P_1(x_1) \cdot P_2(x_2). \tag{3.8}$$

The transformation is simply found as

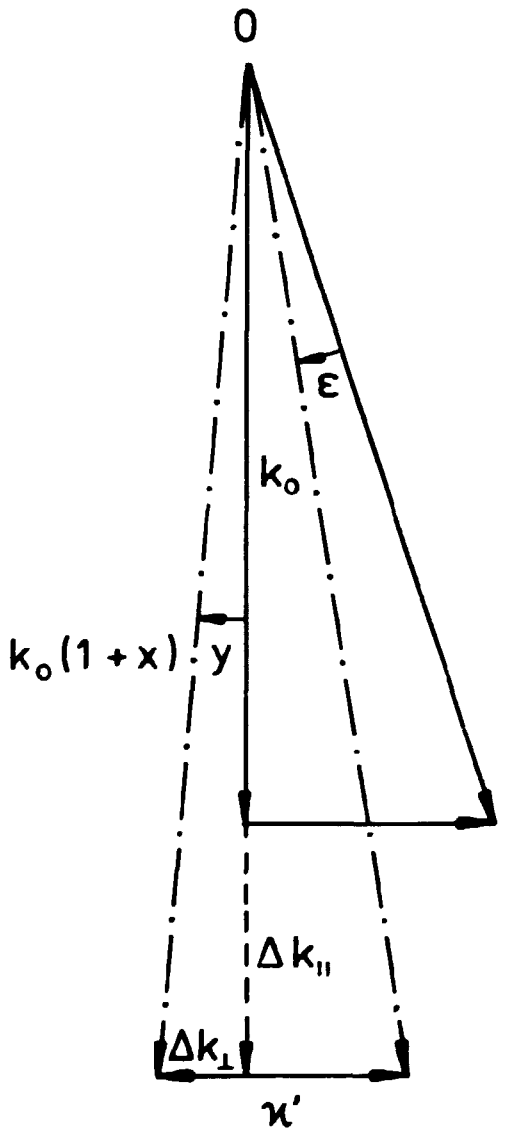

Fig. 3.6. Calculation of the contributions to the resolution function from the velocity selector. The definitions of the parameters in eq. (3.3)-(3.6) are obvious from this figure.

$$x = x_1 - x_2\left(1+\frac{(\kappa')^2}{k_o^2}\right)^{-\frac{1}{2}}$$

$$y = x_2\left(1+\frac{(k_o)^2}{(\kappa')^2}\right)^{-\frac{1}{2}} \qquad (3.9)$$

and hence

$$P_1 = \exp(-(x_1/\{\sigma_1 \cdot k_o/\kappa'\})^2)$$

$$P_2 = \exp(-(x_2/\{\sigma_2\left(1+\frac{k_o^2}{(\kappa')^2}\right)^{\frac{1}{2}}\})^2). \tag{3.10}$$

Hereby the two independent contributions to R_1 are calculated

$$|\bar{X}_1| = k_o \cdot \sigma_1 \frac{k_o}{\kappa'} \qquad \alpha_1 = 0$$

$$|\bar{X}_2| = k_o \cdot \sigma_2\left(1+\frac{k_o^2}{(\kappa')^2}\right)^{\frac{1}{2}} \quad \tan\alpha_2 = -\frac{\kappa'}{k_o} \tag{3.11}$$

$\bar{X}_1$ describes the contribution along k_o assuming infinitesimal collimation before the velocity selector, and $\bar{X}_2$ describes the smearing of this distribution due to the finite collimation before the velocity selector.

The tilt angle α_t is small and

$$\alpha_t = \frac{\kappa'}{k_o} . \tag{3.12}$$

The formulas for $\bar{X}_1$ and $\bar{X}_2$ can be rewritten as

$$|\bar{X}_1| = \frac{k_o \cdot \sigma_1}{\alpha_t} \qquad \alpha_1' = 0$$

$$|\bar{X}_2| = k_o \cdot \sigma_2 \cdot (1+\alpha^2)^{\frac{1}{2}} \qquad \alpha_2' \simeq -\alpha_t \tag{3.13}$$

As $\alpha_t << 1$ and $\sigma_1 \simeq \sigma_2$, then

$$|Y_1| \sim 0$$

$$|Y_2| \simeq \frac{k_o \cdot \sigma_1}{\alpha_t} \qquad \alpha' = \theta \tag{3.14}$$

and transformation to $\bar{Z}_1$ and $\bar{Z}_2$ yields

$$|z_1| = 0$$
$$|z_2| = \frac{k_o \cdot \sigma_1}{\alpha_t} \cdot \sin\alpha' \approx k_o \cdot \sigma_1 \tag{3.15}$$

and

$$|z_1|_{incl} = k_o \cdot \sigma_3 . \tag{3.16}$$

Finally, one finds

$$R_\parallel = 2k_o \left(\frac{\sigma_3^2 \cdot \sigma_1^2}{\sigma_3^2 + \sigma_1^2} \right)^{\frac{1}{2}}$$
$$R_\perp = 2\kappa \left(\frac{\sigma_3^2 \cdot \sigma_1^2}{\sigma_3^2 + \sigma_1^2} \right)^{\frac{1}{2}} \tag{3.17}$$

or, because $\sigma_3 << \sigma_1$,

$$R_\parallel = 2k_o \cdot \sigma_3$$
$$R_\perp = 2\kappa \cdot \sigma_3 . \tag{3.18}$$

The collimation before the velocity selector is a result of the neutrons passing through a neutron guide tube, and σ_2 is given by the critical angle for total reflection in the guide tube (Ni-coated)

$$\sigma_2 = \theta_c = \frac{36.8}{k_o (\text{Å}^{-1})} \text{ arc min.}$$

The dimensions of the velocity selector are given in the caption below fig. 3.5 and

$$\sigma_1 = 20' ,$$

$$\kappa = .000829 \; \nu \text{ (rps)} \quad (\text{Å}^{-1}) ,$$

$$k_o = .000829 \; \frac{\nu \text{(rps)}}{\alpha_t \text{(rad)}} (\text{Å}^{-1}) .$$

For α_t = .02 radian and ν = 43 rps,

$$k_o = 1.8 \text{ Å}^{-1}$$

and thus

$$\sigma_2 \simeq 20' .$$

The distance from the sample to the detector (ℓ_2 in fig. 3.4) can be chosen up to 40 m (the instrument at the Institut Laue-Langevin). The sample mask and the detector element would typically be 1 cm x 1 cm. Thus, for ℓ_2 = 8 m, one finds

$$\sigma_3 = 4'$$

and

$$R_{\parallel} = 4.5 \cdot 10^{-3} \text{ Å}^{-1}$$

$$R_{\perp} = 2.5 \cdot 10^{-3} \cdot \kappa .$$

SAS's have been constructed at several major neutron scattering centers and they have a wide area of applications ranging from solid state physics through metallurgy and chemistry to biology, see the Procedings from the 3. international conference on small angle scattering (e.g. Schmatz et al, 1974).

3.4. Resumé of the chapters 2 and 3

Some principles of small angle scattering techniques have been discussed. It is shown that the resolution function has a pathological anisotropic shape near the forward direction provided narrow collimations before and after the sample. The width of the resolution function is always extremly small in the direction perpendicular to the momentum transfer vector while the width in the parallel direction only can be considered as small if the dimensions of the reciprocal space of the sample is sufficiently large compared with the wavevector of the radiation probe.

Thus all small angle scattering instruments are characterized by extreme narrow collimator systems. The narrow collimation can be obtained either by using perfect crystals or by extending the distances from radiation source to sample and from sample to detector.

These two possible methods are exhaustive for the available general collimator systems. All specific designs will be variation of these two. Examples have been given in the proceding sections. The characteristics of these instruments are summed up in the table 3.1 below. The rest of the report gives examples of the use of the instruments.

Table 3.1. Characteristics of the instruments described in chapters 2 and 3.

Instrument	Radiation	Collimation method	Size of instrument m	Typical wave vector $Å^{-1}$	κ min $Å^{-1}$	$R_\perp/\kappa$	$R_\parallel$ $Å^{-1}$
TAS (small angle limit)	Neutrons	Soller collimators	2.5	1.55	0.02	$4\cdot10^{-3}$	$6\cdot10^{-3}$
DCS	Neutrons	Perfect Si-crystals	2.5	1.55	$4\cdot10^{-4}$	$2\cdot10^{-5}$	10^{-4}
GAD	412 keV γ-rays	Slit collimators	6	210	"large"	$7\cdot10^{-5}$	0.02
SAS	Neutrons	Slit collimators	10-50	1.55	0.01	$2\cdot10^{-3}$	$4\cdot10^{-3}$

4. STUDY OF THE ORDER-PARAMETER NEAR THE JAHN-TELLER TRANSITION IN $TbVO_4$, $DyVO_4$ and $DyAsO_4$.

The rare earth (RE) vanadates and arsenates, where the RE is Tb, Tm or Dy, exhibit at low temperatures a structural phase transition from the tetragonal zircon structure (space group D_{4h}^{19}) to

the orthorhombic structures D_{2h}^{24} for the Tb and Tm compounds and D_{2h}^{28} for the Dy compounds. These transitions have been subject to extensive theoretical and experimental studies (G.A. Gehring and K.A. Gehring 1975, R.T. Harley 1977, and J.K. Kjems 1977), and it has been established that the transitions are of the cooperative Jahn-Teller type, i.e., driven by a coupling of the lowest electronic levels of the RE ion to the lattice distortion.

Using neutron and γ-ray diffraction the static lattice distortion in $TbVO_4$, $DyVO_4$ and $DyAsO_4$ was studied. The results of birefringence measurements (R.T. Harley et al. 1975 and R.T. Harley, private communication) were confirmed. In $TbVO_4$ (T_D = 33.2 K), there is an excellent agreement between the experimental results and a simple mean field theory. $DyVO_4$ (T_D = 14.4 K) appears to give a non-classical order parameter exponent, β = 0.34, over a wide temperature range. Finally, in $DyAsO_4$ (T_D = 11.3 K) the phase transition is of first order. The results are seen in fig. 4.1 and will be further discussed in the following sections.

Following the theory of Elliott et al. (R.J. Elliott et al. 1972), the transitions can be discussed in terms of a pseudo-spin-phonon coupling mechanism leading to the 3-D Ising model with a transverse field. The molecular field theory applied to this model is in quantitative agreement with the experimental results for the Tb and Tm compounds. In order to understand the behaviour of $DyVO_4$ it is necessary to assume that the dominant interaction in this compound is of short range. Several experimental findings have been used as evidence for this viewpoint. (R.T. Harley et al. 1975). However, the theory does not show any first order transition as found in $DyAsO_4$. This point was the main motivation for suggesting an alternative approach. The phase transitions are considered in the light of a phenomenological Landau theory, and it is proposed that the family of RE zircons is a system with tricritical behaviour. In this setting the Tb and Tm compounds would be far from the tricritical point on the second order transition side. $DyVO_4$ would be close to the tricritical point, but still with a second order transition, and $DyAsO_4$ would be beyond the tricritical point on the first-order side.

As will be discussed later, several observations - among them some used as evidence for the dominant short range interaction in $DyVO_4$ - lend support to this approach. It is at present not clear which mechanism is responsible for this behaviour, but some characteristics can be deduced from the phenomenological theory.

4.1. Experimental results

The three samples for this study were grown at the Clarendon Laboratory. They were shaped as rectangular parallelepipeds and were approximately 1 mm x 1 mm x 4 mm in size. They grow with the c-axis parallel to the largest dimension and the a-axis along the crystal faces.

Care must be taken when mounting the samples in the cryostat in order to obtain a mounting without external stress. The samples were wrapped in thin Al-foil and glued at one of the foil ends to the sample holder.

The temperature was measured with a germanium resistor and the temperature stability was $\pm$ 0.05 K.

In $TbVO_4$ the lattice distortion is a shear mode of B_{2g} symmetry. In an elastic scattering experiment it manifests itself as a splitting of the (h00) Bragg reflection along the (0l0) direction. Thus the splitting was measured from rock scans through the (200) Bragg reflection. The neutron energy in these experiments was 13.7 meV and the horizontal collimations 15 min. of arc.

In the Dy compounds the lattice distortion is of B_{1g} symmetry. This distortion will be seen as a splitting of the (h00) reflections along the (100) direction and/or a splitting of the (hh0) reflection along the $(\bar{1}10)$ direction. In the experiments the latter distortion was observed, and because of the accidentally small (220) structure factor the splitting was measured from scans through the (200) reflection along the $(\bar{1}10)$ direc-

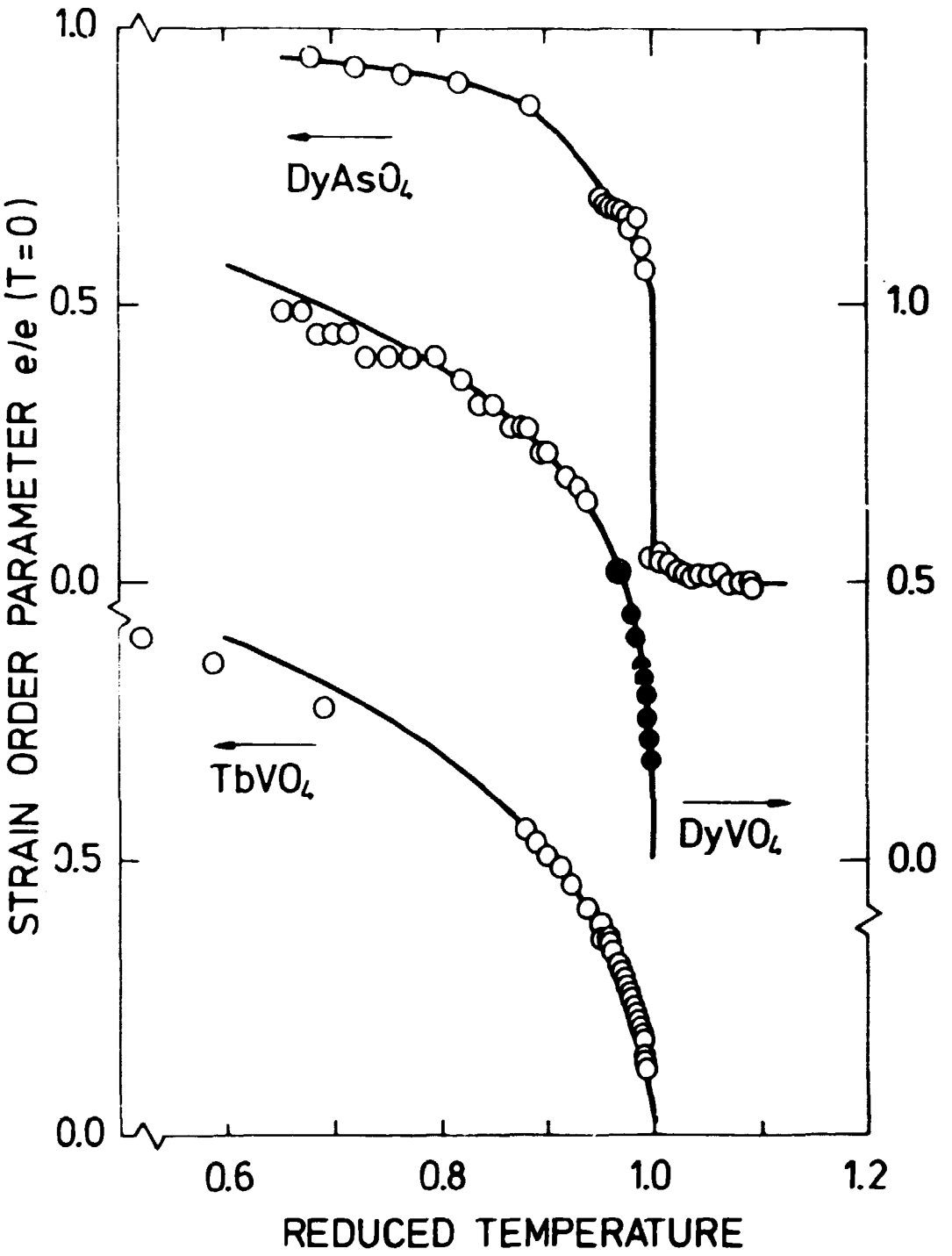

Fig. 4.1. The strain order parameter in $TbVO_4$ (T_D = 33.22 K), $DyVO_4$ (T_D = 14.42 K) and $DyAsO_4$ (T_D = 11.28 K) as a function of the normalized temperature. The open points are the neutron scattering data of this work. The full points are birefringence data obtained by Harley et al. (1975).

tion. The neutron energy was chosen to optimize the resolution. With a graphite monochromator and a neutron energy of approximately 5 meV, a parallel-parallel configuration was obtained. The $DyAsO_4$ sample distorted as a single domain.

The main results are shown in fig. 4.1. The temperature scales have been normalized by the transition temperatures. The strain scales have been normalized by the saturation strain, e, at T = 0 K. For $TbVO_4$, e_6 (= 2 e_{ab}) = .0239±.0002 and for $DyVO_4$ and $DyAsO_4$, respectively, e_1 (= e_{aa}) = .0023±.0001, .0017±.0001 at T = 0 K. The full points in the $DyVO_4$ curve are data obtained by birefringence (R.T. Harley et al. 1975) scaled to our data at T/T_D = 0.981. The full curves through the $TbVO_4$ and $DyVO_4$ data are theoretical curves to be discussed later. A "guide-to-the-eye"-curve is shown through the $DyAsO_4$ data. The transition temperatures were measured independently by the extinction release method.

$TbVO_4$ and $DyVO_4$ were also studied using the GAD. These measurements did not add new information to the neutron data obtained below T_D. Above T_D, we observed a precurser effect as earlier reported for $TmAsO_4$ (K. Møllenbach et al. 1977). As T_D is approached from above the Bragg-intensity decreases without any hysteresis effects. This is believed to be an extinction effect resulting from fluctuations in the mosaic structure of the sample. It might also affect the analysis of central peak scattering data such as those obtained by Hutchings et al. (1975) for $TbVO_4$.

4.2. The Landau Theory

In this section the phase transitions in the RE-zircons are discussed in terms of a Landau theory having purely phenomenological parameters. This approach is very similar to the theory for ferroelectrics proposed by Devonshire (Fatuzzo and Merz 1967).

The first part of the Landau theory Ansatz states that the Helmholz potential can be expanded in powers of a general order parameter Q close to the transition temperature. In the actual case Q must implicitly describe the splitting of low lying degenerate or near degenerate states and the non-zero strain. It will be clear later that Q is equivalent to the pseudo-spin in the theory of Elliott et al. (1972). The Helmholz potential per unit volume is given by

$$A = A_o + \frac{k_B}{V_o} (\alpha Q^2+\beta Q^4+\gamma Q^6-\varepsilon eQ+\delta e^2) \qquad (4.1)$$

In this expression the two terms extracted from the general power series in Q are easily recognized. The first describes the coupling between the strain and the general order parameter Q and the second term is the elastic energy in the absence of the Jahn-Teller coupling. Because of symmetry only even powers in the order parameter appear.

The equilibrium condition is $\frac{\partial A}{\partial Q} = 0$, yielding

$$2\alpha Q-\varepsilon e + 4\beta Q^3 + 6\gamma Q^5 = 0 \qquad (4.2)$$

The stress is given by

$$S = \frac{\delta A}{\delta e} = (2\delta e - \varepsilon Q) \cdot \frac{k_B}{V_o} \qquad (4.3)$$

If $S = 0$, then

$$e = \frac{\varepsilon}{2\delta} Q = k \cdot Q \qquad (4.4)$$

and (4.1) can be rewritten as

$$A = a(T-T_D)k^2 \cdot e^2 + bk^4 \cdot e^4 + ck^6 \cdot e^6 \qquad (4.5)$$

with

$$a(T-T_D) = \alpha - \frac{\varepsilon^2}{4\delta}, \quad b = \beta \quad \text{and } c = \gamma, \quad k = \frac{\varepsilon}{2\delta}$$

Hereby it is indicated that near the transition temperature T_D the coefficient at the second order term is linear in the temperature and b and c are temperature independent. This is the second part of the Landau theory Ansatz. a,b,c and T_D can, however, all depend on other parameters, e.g., some external field. The equilibrium condition, the equation of state, shows for zero stress the following: above T_D, the order parameter is zero and below T_D it attains a non-zero value.

The phase transition will be of second order if the coefficient $b > 0$, and close to the transition temperature the order parameter will be proportional to the square root of the reduced temperature, i.e., the critical exponent $\beta = .50$. If $b < 0$ the phase transition will be of first order.

A system exhibits a tricritical behaviour if a monotonical change of some parameter can drive b from a positive to a negative value. The tricritical point is the point at which $b = 0$. At this point the order parameter will be proportional to the fourth root of the reduced temperature, i.e., the critical exponent $\beta = 0.25$. For $b > 0$, it is important to notice that as b becomes smaller relative to c, the temperature range in which $\beta = 0.50$ can be observed shrinks.

Several observable thermodynamic properties can be calculated from the Helmholz potential. In the following, b is assumed to be positive and the stress is zero or in the zero limit.

First the explicit value of the order parameter below T_D is found from (4.5)

$$e = \left(\frac{b}{3ck^2}\left(\left(1 - \frac{3ca}{b^2}(T-T_D)\right)^{\frac{1}{2}} - 1\right)\right) \quad T < T_D \; . \tag{4.6}$$

The entropy is given by

$$S = -\frac{\partial A}{\partial T} = -ak^2 \cdot e^2 \cdot \frac{k_B}{V_o} \tag{4.7}$$

and thus the specific heat associated with the strain is zero above T_D and below T_D

Table 4.1. The coefficient in the Landau free energy expansion found from the measurement using equations 9, 10, and 11.

	T_D	k	$\frac{2b}{e}$	$\frac{3c}{a}$	$\frac{a^2}{2b} T_D$	a	b	c	$C^{elast}/(T-T_D) = 2\frac{k_B}{V_o}ak^2$, $(T>T_D)$ calc. dyn/cm^2/K	meas.
$TbVO_4$	33.22	41.9±0.4	11.2±0.1	6.8±0.2	1.5*	0.50±0.03	2.8±0.2	1.1±0.1	$(3.0\pm0.2)\cdot10^9$	$2.8\cdot10^{9}$***
$DyVO_4$	14.42	435±20	0.6±0.1	3.9±0.5	4**	0.17±0.03	0.06±0.02	0.23±0.07	$(1.2\pm0.3)\cdot10^{11}$	$1.1\cdot10^{11}$***

* from Wells et al. (1972)

** from Cooke et al. (1971)

*** from Sandercock et al. (1972)

$$C^{heat} = T\frac{\partial S}{\partial T} = \frac{a^2}{2b}\cdot T\left(1 - \frac{3ac}{b}(T-T_D)\right)^{-\frac{1}{2}}\cdot R \ , \ T < T_D \qquad (4.8)$$

where R is the gas constant.

At $T = T_D$ the discontinuous jump is

$$\Delta C^{heat} = \frac{a^2}{2b}\cdot T_D \cdot R \qquad (4.9)$$

The elastic constant is the derivative of the stress with respect to the strain and close to T_D it is given by

$$C^{elas} = \begin{cases} 2\frac{k_B}{V_o}\, ak^2(T-T_D) & T > T_D \\ 4\frac{k}{V_o}\, ak^2(T_D-T) & T < T_D \end{cases} \qquad (4.10)$$

It is thus clear that a,b,c,T_D and k can be deduced from relatively few experiments. They are summed up here.

T_D can be measured directly. A measurement of the strain versus the temperature can be fitted to a curve

$$T = T_D - \frac{2b}{a}k^2\cdot e^2 - \frac{3c}{a}k^4 e^4 \qquad (4.11)$$

yielding two equations for the parameters. k is found from the inverse value of the saturation strain

$$k = e(T = 0)^{-1}$$

Two more equations among the parameters are given by the specific heat jump at T_D and the slope of the elastic constant at T_D. Altogether this gives 5 independent equations to find 4 parameters, so these experiments will not only give the parameters but also a consistency check.

This analysis has been applied to $TbVO_4$ and $DyVO_4$. The strain measurement from the previous section has been used together with the earlier reported measurements of specific heat (M.R. Wells et al. 1972, A.H. Cooke et al. 1971) for finding the parameters a,b, and c. The results are shown in table 4.1. As a con-

sistency check the elastic constants were calculated and compared with measurements (J.R. Sandercock et al. 1972). It should be noted that the elastic constants calculated from the phenomenological theory are isothermal elastic constants.

The full curves in fig. 4.1 are calculated from eq. (4.11) with the parameter values from table 4.1. To be able to examine the temperatures close to T_D, the same curves are shown in fig. 4.2 as a log-log plot of the absolute strain versus the reduced

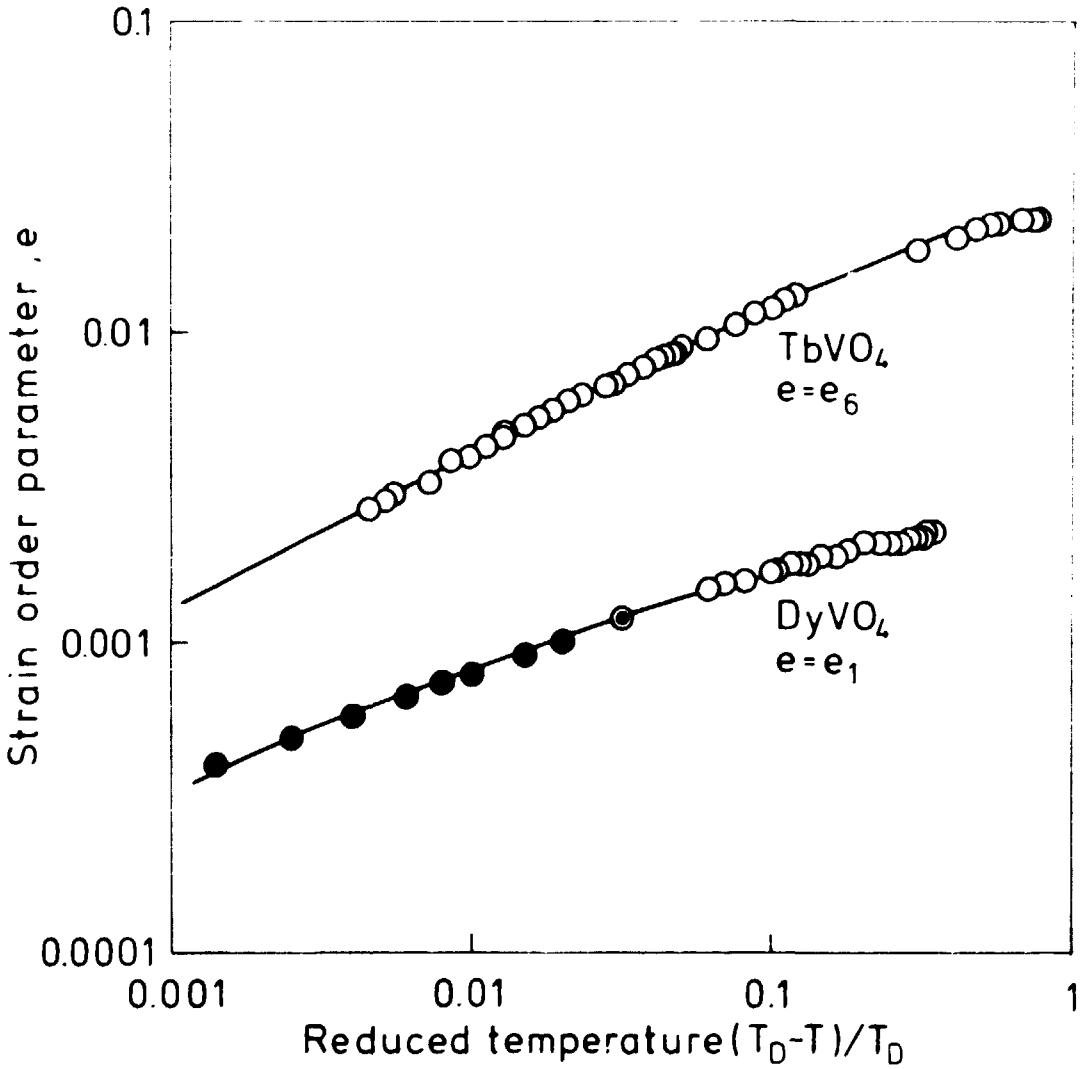

Fig. 4.2. The strain order parameter in $TbVO_4$ and $DyVO_4$ as a function of the reduced temperature. The full curves are the results of the Landau theory analysis.

temperature $t = (T_D-T)/T_D$. From table 1 it is seen that, for $DyVO_4$, b is smaller relative to a and c than for $TbVO_4$. As a result the temperature region in which a classical behaviour of the order parameter can be observed is much narrower for $DyVO_4$ than for $TbVO_4$, as can be seen from fig. 4.2.

Calculation of thermodynamic properties can of course also be carried out for $b < 0$, i.e. a first order transition. This will introduce new parameters, e.g. a temperature region with a metastable state, but the available data are insufficient for analyzing $DyAsO_4$ in this scheme. Thus one can only state that, for $DyAsO_4$, b is negative.

However, these findings for the variation of b through the family of RE zircons suggest that this group of compounds may exhibit a tricritical behaviour with $TbVO_4$ far from and $DyVO_4$ close to the tricritical point on the second-order transition side, and $DyAsO_4$ beyond the tricritical point on the first order transition side.

For this conclusion to hold, it is still necessary to justify why this very simple theory should be applicable to these compounds and for this reason a discussion of the critical fluctuations is made.

4.3. The anisotropic fluctuations

A renormalization group study of acoustic phonon instabilities has been made by Cowley (R.A. Cowley 1976). This author points out that in systems with the tetragonal symmetry of interest here, the phase transitions will be of second order provided that the part of the interactions quartic in the strain order parameter is positive. Because the fluctuations are highly anisotropic the marginal dimensionality will be $d^* = 2$ for these systems indicating that the Landau theory is selfconsistent for real 3-dimensional systems. Thus the renormalization group analysis justifies the simple data analysis in the previous section. In the following the anisotropic fluctuations are discussed

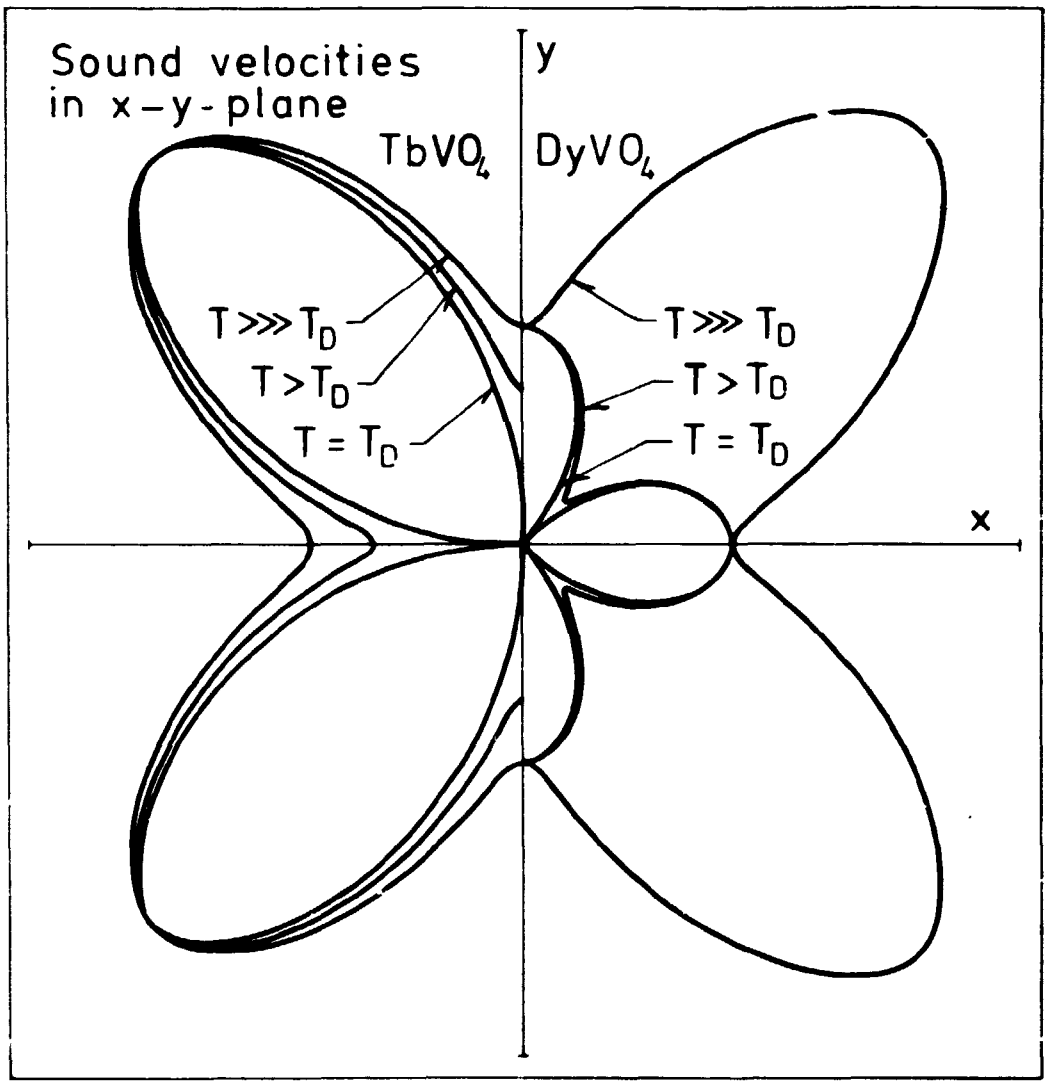

Fig. 4.3. The sound velocities in the x-y plane of $TbVO_4$ (left hand side) and $DyVO_4$ (right hand side) at three different temperatures. This gives a semi-quantitative picture of the change in anisotropy of the fluctuations as T_D is approached since the strength of the fluctuations is inversely proportional to the sound velocities. The curves are based on the measurements by Sanderock et al. (1972).

and some of the physics responsible for the very narrow "classical" temperature range in $DyVO_4$ revealed. A semi-quantitative understanding of the fluctuations can be obtained from studying the sound-velocities in the ab-plane as a function of propagation direction.

From the Christoffel equation for a tetragonal system, it is straight forward to calculate the sound velocities,

$$(c_{44}-\rho v^2)\{(\rho v^2)^2-(\rho v^2)(c_{11}+c_{66}) + c_{11}c_{66}+\ell^2m^2(c_{11}-c_{12}-2c_{66})(c_{11}+c_{12})\} = 0 \qquad (4.12)$$

where ρ is the density, v is the sound velocity, ℓ and m are direction cosines, and c_{ij} denotes the elastic constants in Voigt's notation.

The root $\rho v^2 = c_{44}$ is a pure transverse mode independent of propagation direction. The other two modes are in general mixed modes given by

$$\rho v^2 = \tfrac{1}{2}(c_{11}+c_{66}) \pm \{\tfrac{1}{4}(c_{11}+c_{66})^2 - (c_{11}-c_{12}-2c_{66})(c_{11}+c_{12})\ell^2m^2\}^{\frac{1}{2}} \qquad (4.13)$$

In the (100) and (110) directions the modes become pure. The transverse mode corresponds to the minus-sign in equation (4.13). For the (100) and the (110) directions respectively one finds $\rho v^2 = c_{66}$ and $\rho v^2 = \tfrac{1}{2}(c_{11}-c_{12})$ respectively.

As mentioned previously, the elastic constants have been measured (J.R. Sandercock et al. 1972). From these results the minus-sign root in equation (4.13) is plotted as a function of propagation direction. This plot is seen in fig. 4.3 for three temperatures. The left hand side shows the behaviour for $TbVO_4$ and the right hand side for $DyVO_4$.

The strength of the fluctuations is inversely proportional to the sound velocity in a given direction and hence fig. 4.3 is a

semi-quantitative picture of the inverse of the fluctuations, and most importantly it shows the anisotropy of the fluctuations and the change in anisotropy as a function of temperature. As seen from equation (4.13), the anisotropy is given by the ratio between c_{66} and $\frac{1}{2}(c_{11}-c_{12})$.

Since the anisotropy of the fluctuations is responsible for the "classical" behaviour of $TbVO_4$ and $DyVO_4$ it is expected that the temperature regions in which this behaviour is seen will

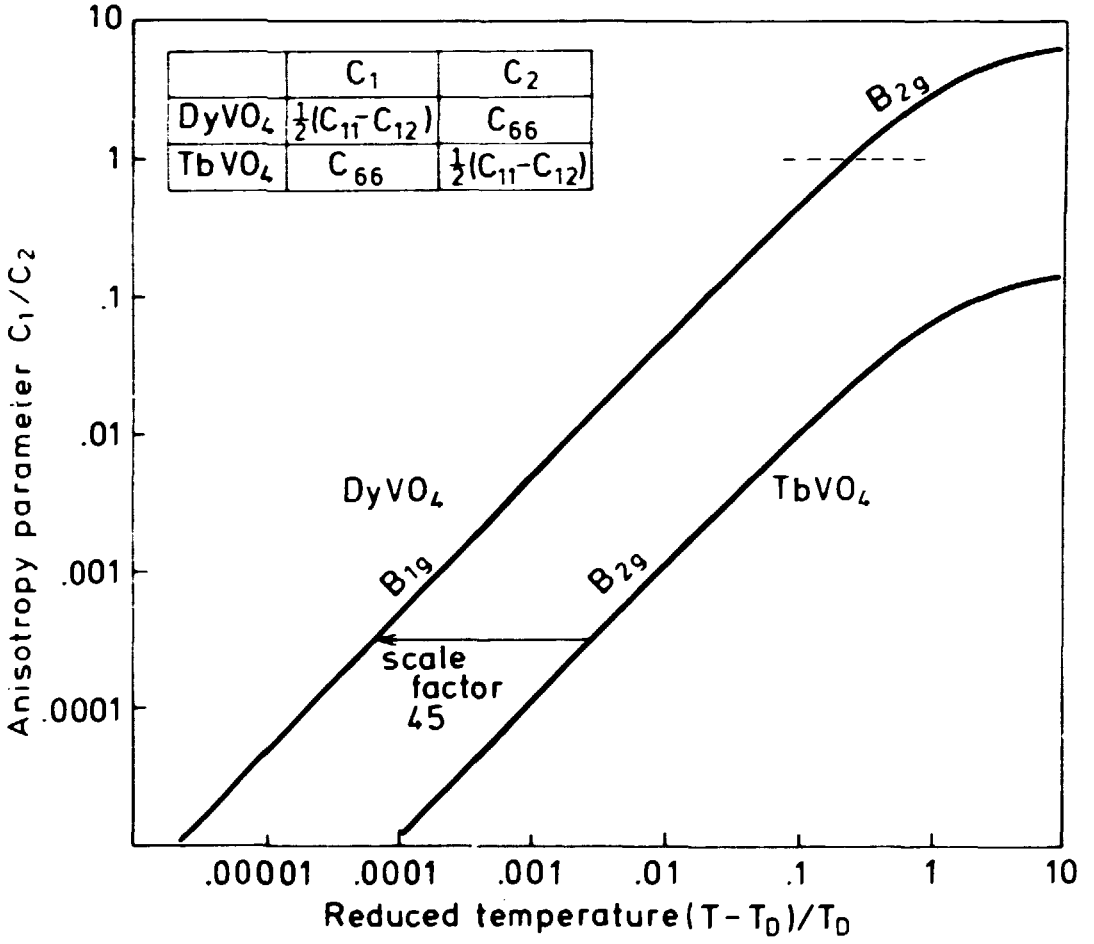

Fig. 4.4. The anisotropy parameter c_1/c_2 versus reduced temperature for $TbVO_4$ and $DyVO_4$ based on the measurements by Sandercock et al. (1972). It shows that the temperature region where the true critical exponents can be measured is 45 times smaller for $DyVO_4$ than for $TbVO_4$.

scale with the temperature regions in which the systems experience the same relative change in anisotropy. Figure 4.4 is a plot of the ratio between the elastic constants c_{66} and $\frac{1}{2}(c_{11}-c_{12})$ and it illustrates the change in anisotropy in the fluctuations above the transition temperature. It can directly be seen that in units of reduced temperature the temperature region in which $DyVO_4$ will exhibit "classical" behaviour is 45 times as narrow as the region in $TbVO_4$. Thus when the power law $e \propto t^{\beta}$ is valid for, say, $t < 0.1$ in $TbVO_4$ it will only be valid in $DyVO_4$ for $t < 0.002$.

This observation is in good agreement with the results found from analyzing the strain measurements in the simple Landau picture although no direct observations at $t < 0.002$ were made. In a neutron scattering experiment it was not possible to make these measurements because of the limited instrumental resolution, and in a γ-ray diffraction experiment sample imperfections limited the effective resolution. It might, however, be possible to pursue the ideas in this section by means of high resolution, x-ray measurements.

4.4. Calculations based on the microscopic theory

The coefficients used in the Landau theory are purely phenomenological. Here an attempt is made to gain an insight in the physics underlying the coefficient by calculations from the microscopic theory of Elliott et al. (1972).

The starting point is the mean field Hamiltonian

$$H = -\Delta \cdot \sigma^{x} - (\lambda < \sigma^{z} > + \eta e)\sigma^{z}$$

which is the 3d-Ising Hamiltonian in a transverse field. This is the Hamiltonian for the two level model of $DyVO_4$. It is applicable to the Dy and Tm compounds but strictly speaking not to the Tb compounds. However, the results will also be applied to $TbVO_4$ in order to simplify the discussion.

Δ - the transverse field - is the splitting of the two levels above T_D. Δ is zero for $TbVO_4$ and non-zero for $DyVO_4$. λ describes the phonon coupling and η the coupling to the strain. The energy of the two levels are $\pm W$ where $W = \{(\lambda<\sigma^z>+\eta e)^2+\Delta^2\}^{\frac{1}{2}}$.

The Helmholz energy is

$$A = A_o - \tfrac{1}{2}\frac{1}{V_o}\lambda<\sigma^z>^2 - \frac{1}{V_o}\eta<\sigma_z>\cdot e + \tfrac{1}{2}ce^2 \qquad (4.14)$$

$$+ \frac{k_B T}{V_o}\frac{W}{(\lambda+\mu)}\tanh^{-1}\left(\frac{W}{(\lambda+\mu)}\right) + \tfrac{1}{2}\frac{k_B T}{V_o}\ln\left(1-\left(\frac{W}{(\lambda+\mu)}\right)^2\right)$$

where the zero stress condition $\frac{\partial A}{\partial e} = 0$ has been used to introduce the constant

$$\mu = \frac{2\eta^2}{V_o c} \qquad (4.15)$$

so that

$$e = \frac{\mu}{\eta} < \sigma^z > \qquad (4.16)$$

At zero temperature the level energy is

$$(\lambda+\mu) = \{(\lambda+\mu)^2 < \sigma^z\ (T=0)\ >^2 + \Delta^2\}^{\frac{1}{2}} \qquad (4.17)$$

or

$$< \sigma^z(T=0) > = \frac{((\lambda+\mu)^2-\Delta^2)^{\frac{1}{2}}}{(\lambda+\mu)} \qquad (4.18)$$

Now the order parameter Q is introduced identical to the general order parameter in the Landau expansion and $<\sigma^z>$ is at non-zero temperatures given by

$$<\sigma^z> = Q\cdot\frac{((\lambda+\mu)^2-\Delta^2)^{\frac{1}{2}}}{(\lambda+\mu)} = Q\cdot(1-y^2)^{\frac{1}{2}} \qquad (4.19)$$

The Helmholz energy can through a lengthy but straightforward (see Appendix B) calculation be expanded in powers of Q

$$A = A_o + \frac{k_B}{V_o}(a(T-T_D)\cdot Q^2 + b\cdot Q^4 + c\cdot Q^6) \qquad (4.20)$$

with

$$a = \tfrac{1}{2}\,\frac{\tanh^{-1}y}{y}\cdot(1-y^2)$$

$$b = T\,\frac{1}{8}\left\{\frac{1}{1-y^2} - \frac{\tanh^{-1}y}{y^3} + \frac{1}{y^2}\right\}\cdot(1-y^2)^2 \qquad (4.21)$$

$$c = T\cdot\frac{1}{48}\left\{2\frac{y^2}{(1-y^2)^2} + \frac{1}{1-y^2} + \frac{3}{y^5}\left(\tanh^{-1}y - y - \frac{y^3}{3}\right)\right\}\cdot(1-y^2)^3$$

From these equations a,b,c are calculated and compared with the values found in the data analysis. In the calculations of b and c the parameters have the following values: $T = T_D$, $y = 0$ for $TbVO_4$ and $y = 0.33$ for $DyVO_4$. The last figure is found from the values of λ, η and Λ earlier reported (Gehring et al. 1972). The results are seen in table 4.2.

Table 4.2

		a	b	c
$TbVO_4$	measured (Table 4.1)	0.50±0.03	2.8±0.2	1.1±0.1
	calculated (eq. 4.21)	0.50	2.77	1.11
$DyVO_4$	measured (Table 4.1)	0.17±0.3	0.06±0.02	0.23±0.07
	calculated (eq. 4.21)	0.46	1.1	0.44

The agreement between the calculated and measured coefficients for $TbVO_4$ are striking. For $DyVO_4$ all the calculated coefficients are much greater than the measured. From the equations for the coefficients it is further obvious that the microscopic model cannot drive a first order transition. These facts seem to point out that an important mechanism has not been properly accounted for in the microscopic theory for the Dy compounds while $TbVO_4$ is well described by this theory.

4.5. Summary

The strain order parameter near the Jahn-Teller transitions in $TbVO_4$, $DyVO_4$ and $DyAsO_4$ has been analyzed with a simple Landau theory. This phenomenological theory gives a unified picture of the RE zircons as a family of compounds exhibiting a tricritical behaviour.

An important consequence of the phenomenological theory is that the order parameter exponent eventually has the classical value $\beta = 0.50$ at all critical points where a second order transition takes place except at a tricritical point. The statement of this paper is then that $DyVO_4$ is close to a tricritical point and hence that the order parameter in the measurable temperature region is dominated by the 6th order term in the free energy expansion.

The validity of the simple phenomenological approach is plausible from a renormalization group analysis applicable to the RE zircons. Due to the strongly anisotropic fluctuations in the order parameter the marginal dimensionality is reduced to $d^* = 2$. Thus the simple Landau theory is selfconsistent for $d = 3$.

No speculations of the mechanism responsible for the tricritical behaviour are made. However, this behaviour is not surprising since the RE zircons family has a tricritical behaviour with respect to the magnetic properties. (P.A. Lindgaard, Private Communication) Experiments with systems where two Jahn-Teller active ions are mixed might give further data for understanding of the RE zircons.

5. NEUTRON SCATTERING FROM FERROMAGNETIC DOMAINS IN $LiTbF_4$

In the study of critical fluctuations in the dipolar coupled Ising ferromagnet $LiTbF_4$ a strong excess scattering of neutrons very close to the forward direction was observed at temperatures below the ordering temperature by Als-Nielsen (1976a). This chapter reports on a study of this scattering interpreted as originating from the domain structure in the ferromagnetic phase. The scattering was measured partly with the neutron diffractometer in the small angle limit covering momentum transfers, q, in the region $0.01Å^{-1} < q < 0.1Å^{-1}$ (region 1) and partly using the neutron DCS covering the region $0.0005Å^{-1} < q < 0.01Å^{-1}$ (region 2).

The analysis of the data points out that the excess scattering consists of two contributions: one of them is diffraction due to domain-domain correlations and the other one is given by neutron optical effects i.e. refraction and total reflection at domain bounderies. Even though a fairly simple model for the domain structure can be assumed due to the strong anisotropy of the system it is not possible to make a reasonably quantitative calculation of the neutron intensity originating from neutron optical effects and thus a complete separation of the two contributions is not possible. From Monte Carlo calculations it is believed that the measurements in region 2 are totally given by neutron optical effects and that these affect the measurements in region 1 at the smallest values of momentum transfer.

A model for scattering due to domain-domain correlations was developed and tested with the data from the large q-values of region 1. This analysis suggests some interesting physics. The temperature dependence of the data implies that the domain - and domain wall widths are temperature dependent and that the domain structure of the sample would not only be given by the sample size, dislocations etc. but would be related to the thermodynamics of the system.

However the conclusive evidence for this hypothesis is burried in the data from region 2. From the discussion it is clear that the superposition of the two scattering mechanisms are inherent in neutron scattering from magnetic domains and the hypothesis can only be proved or rejected by studies with other experimental methods.

5.1. Experimental results

$LiTbF_4$ orders ferromagnetically at $T_c \sim 2.89K$ with a saturation magnetic moment of the Tb^{3+}-ions of $8.9\mu_B$. The Ising-character is due to the splitting of the $^7F_6$ term of the Tb^{3+}-ion confining the magnetic moments to the c-axis. The dipolar character of the coupling was established by magnetization (L.M. Holmes et al, 1973), neutron scattering (L.M. Holmes et al, 1971) and NMR measurements (P.E. Hansen et al, 1975). $LiTbF_4$ has become the model dipolar-coupled Ising system and it is very well characterized theoretically (A.I. Larkin et al, 1969, A. Aharony, 1973) as well as through measurements of specific heat (G. Ahlers et al, 1975), critical fluctuations (J. Als-Nielsen, 1976a) and spontaneous magnetization (J.A. Griffin et al, 1977).

The theory used in the discussion in sec. 4.3 shows that the strongly anisotropic fluctuations which result from the dipolar coupling reduce the critical dimensionality of the system so that $d^* = 3$ and the critical behaviour of the system is given by the results of the Landau theory with logaritmic corrections (R.A. Cowley, 1976).

The sample for this study was disc-shaped with a thickness of 1 mm and an area 70 mm^2. The z-axis, the Ising-axis, was perpendicular to the disc.

The early measurements showed the domains as elongated objects along the z-axis since the scattering was extremely narrow in the q_z direction and more extended along q_x. Thus the small angle scattering resolution function is well suited for measuring the domain scattering cross-section if the main component of

the momentum transfer vector is kept perpendicular to the Ising axis. It is adequate to study the scattering in the (q_x, q_z)-plane since the scattering proved to be isotropic in the (q_x, q_y)-plane.

The fingerprint of a magnetic origin of neutron scattering is the temperature dependence of the intensity. The origin of the domain scattering was checked in one more experiment. The scattering vanished when a modest magnetic field (e.g. 0.34T at 2.15k) was applied along the Ising axis i.e. the domain structure was destroyed, but the scattering was retained when the field was turned off. No hysteresis was observed. These field measurements were made with a spherical shaped sample.

In region 1 a full dataset $I(q_x,0,0)$ was measured in the temperature region $2.5 \cdot 10^{-3} < t < 7 \cdot 10^{-2}$, where $t = (T_c-T)/T_c$. The ordering temperature was measured independently of the domain scattering by locating the very pronounced peak in the critical scattering at $T = T_c$.

Examples of datasets $I(q_x,0,0)$ are shown in Fig. 5.1 for 8 temperatures. All data have been corrected for background and critical scattering. This contribution to the scattering was measured at temperatures above the critical temperature where the domain scattering has vanished. In this procedure one uses the result found by Als-Nielsen (1976a) that the susceptibility

$$\chi(q,\frac{T}{T_c} - 1, T>T_c) = \chi(q,\tfrac{1}{2}(1-\frac{T}{T_c}), T<T_c).$$

At four temperatures the full intensity profile $I(q_x,q_z)$ was measured. An example is shown in Fig. 5.2 for $T = 2.746K$. These data have been corrected the same way as mentioned above.

The early measurements showed the domains as elongated objects along the z-axis since the scattering was extremely narrow in the q_z direction and more extended along q_x. Thus the small angle scattering resolution function is well suited for measuring the domain scattering cross-section if the main component of the momentum transfer vector is kept perpendicular to the Ising

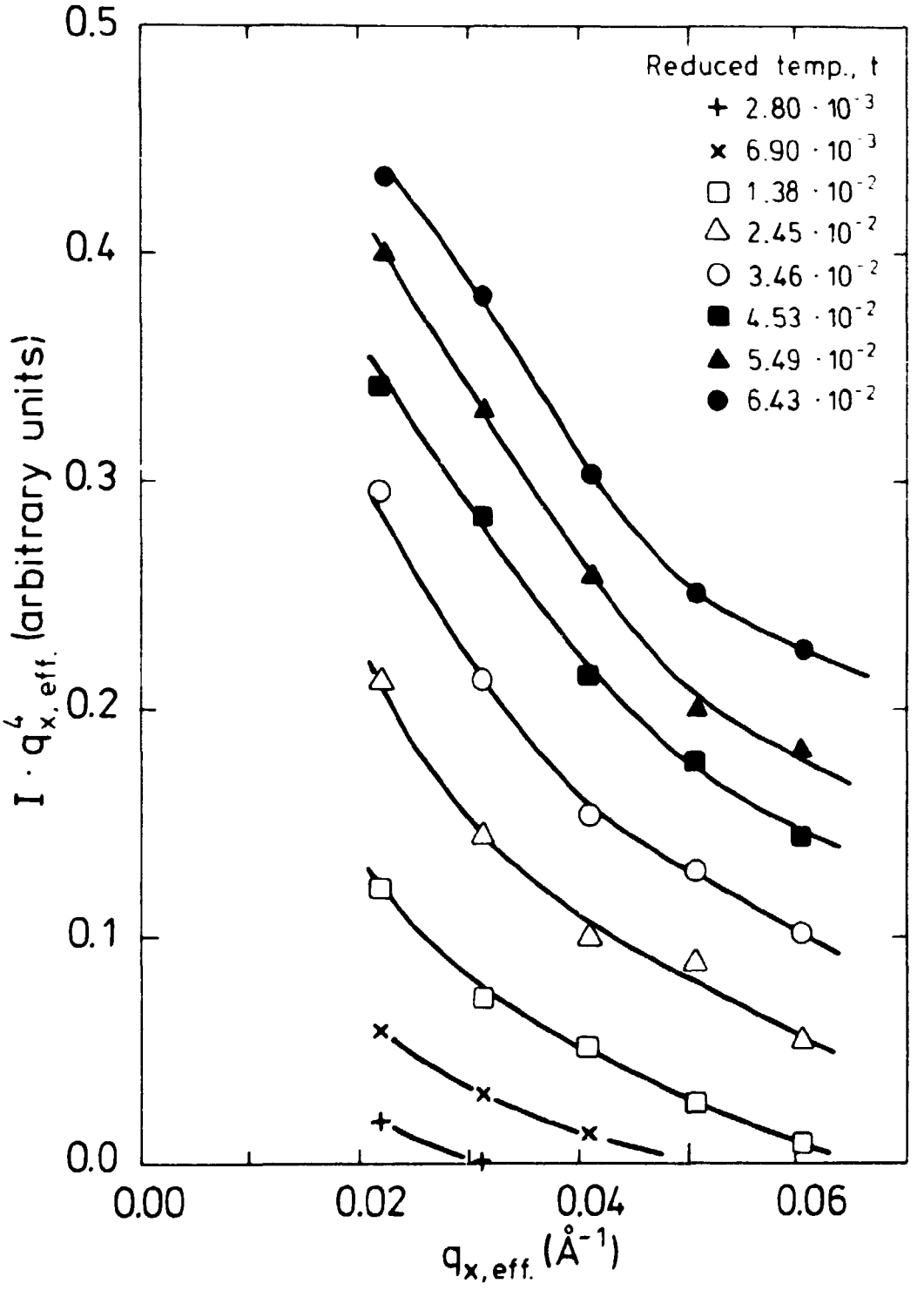

Fig. 5.1. Domain scattering from $LiTbF_4$. Data $I = I(q_x)$ measured by means of a neutron diffractometer in the small angle region. q_x has been replaced by $q_{x,eff}$ - see eq. 5.17. Note: I has been scaled by $q^4_{x,eff}$.

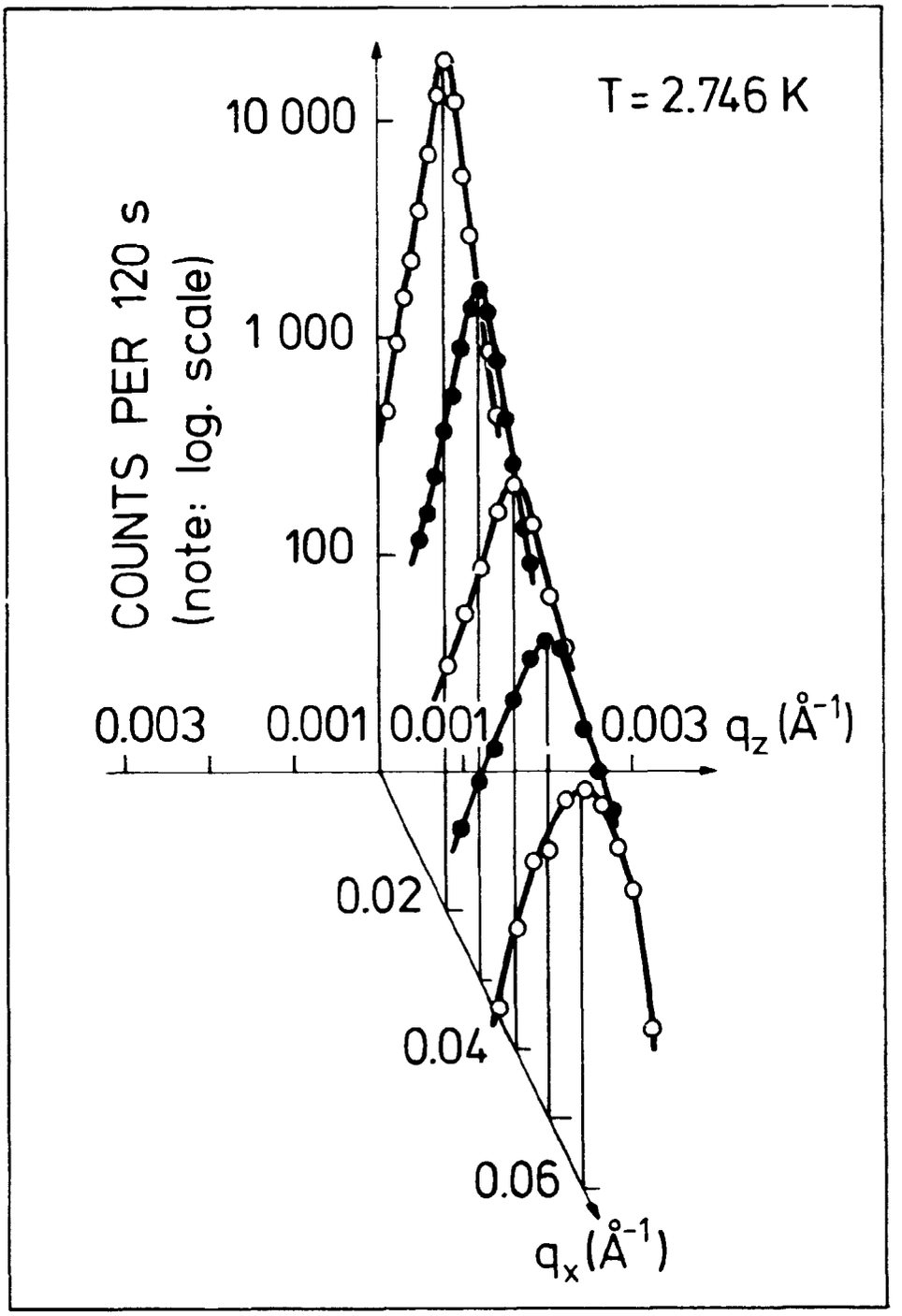

Fig. 5.2. Domain scattering from $LiTbF_4$. An intensity profile $I = I(q_x, q_z)$ for T = 2.746K. Measured by means of a neutron diffractometer in the small angle region. Note the log-scale on the intensity axis.

axis. It is adequate to study the scattering in the (q_x, q_z)-plane since the scattering proved to be isotropic in the (q_x, q_y)-plane.

The fingerprint of a magnetic origin of neutron scattering is the temperature dependence of the intensity. The origin of the domain scattering was checked in one more experiment. The scattering vanished when a modest magnetic field (e.g. 0.34T at 2.15k) was applied along the Ising axis i.e. the domain structure was destroyed, but the scattering was retained when the field was turned off. No hysteresis was observed. These field measurements were made with a spherical shaped sample.

In region 1 a full dataset $I(q_x, q_z = q_y = 0)$ was measured in the temperature region $2.5 \cdot 10^{-3} < t < 7 \cdot 10^{-2}$, where $t = (T_c - T)/T_c$. The ordering temperature was measured independently of the domain scattering by locating the very pronounced peak in the critical scattering at $T = T_c$.

Examples of datasets $I(q_x, q_y = q_z = 0)$ are shown in Fig. 5.1 for 8 temperatures. All data have been corrected for background and critical scattering. This contribution to the scattering was measured at temperatures above the critical temperature where the domain scattering has vanished. In this procedure one uses the result found by Als-Nielsen (1976a) that the susceptibility $\chi(q, \frac{T}{T_c} - 1, T>T_c) = \chi(q, \frac{1}{2}(1-\frac{T}{T_c}), T<T_c)$.

At four temperatures the full intensity profile $I(q_x, q_z)$ was measured. An example is shown in Fig. 5.2 for $T = 2.746K$. These data have been corrected the same way as mentioned above.

Assuming that the main part of the scattering in region 1 can be accounted for by domain-domain correlations then the scattered intensity must have a finite value at $\vec{q} = \vec{o}$ and in some way be described by a characteristic width. It is obvious that an extrapolation to find $I(o,o,o)$ can not be made from Fig. 5.1. With the intension of making this extrapolation possible the domain scattering was measured with a neutron DCS.

An example of an intensity profile at T = 2.865 obtained with this instrument is shown in Fig. 5.3.

The striking features of this figure is the very high scattered intensity relative to the primary beam intensity and the deep valley at small (q_x, q_z). A measurement of the primary beam showed a 90% depletion of primary beam (q_x = o) for small values of q_z. These observations indicate that the scattering in region 2 is given by an almost infinitely large scattering cross-section and the valley in the intensity profile is a result of an extreme extinction effect. The contradiction of the observed infinitely large cross-section and the expected moderately large cross-section leads to a more detailed discussion of the possible mechanisms responsible for the scattering close to the forward direction.

5.2. Refraction or diffraction?*

Consider a single ferromagnetic domain polarized in a given direction in ferromagnetic surroundings polarized in the anti-parallel direction. The domain will give rise to scattering of a neutron beam, but how this scattering is to be treated theoretically is given by the size of the domain, since this property gives the phase change of a neutron on passing the domain.

If this phase change is large compared to that which the neutron would have experienced if the domain had been polarized like its surroundings the scattering can be treated in a continuum picture and the neutron scattering is equivalent to neutron optics. This is one limiting situation called the case of neutron refraction.

If the difference in phase change is small the scattered neutron wave can be treated as a pertubation of the original wave and interactions on an atomic level have to be entered into the

*General reference for the discussion: Bacon (1975)

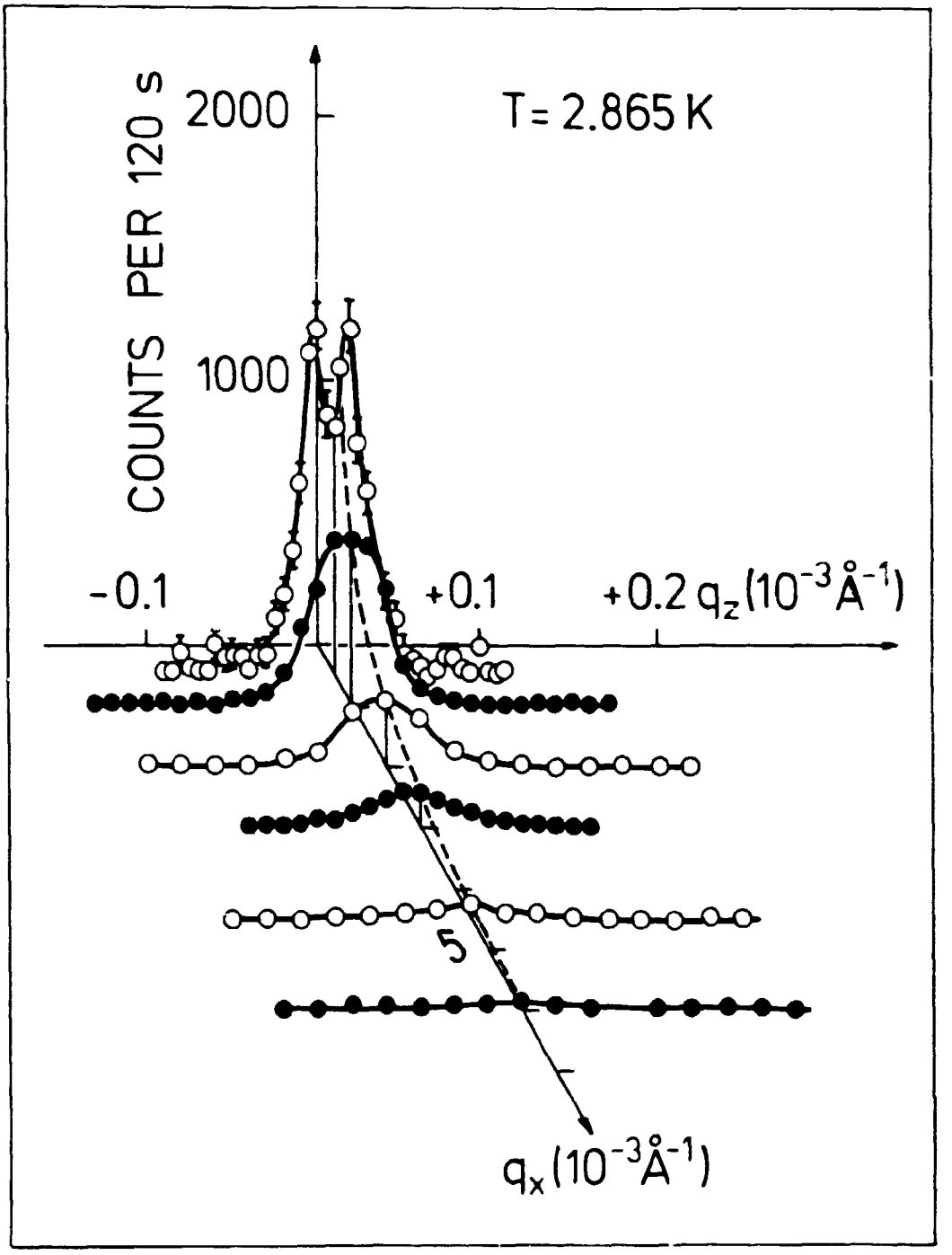

Fig. 5.3. Domain scattering from $LiTbF_4$. An intensity profile $I = I(q_x, q_z)$ for T = 2.865K measured by means of a neutron DCS. Note the units on the q-axis.

calculations. This is another limiting situation called the case of neutron diffraction.

The difference in phase change is given by

$$\varphi = 2k\,(1-n)\cdot R \qquad (5.1)$$

where k is the neutron wave vector, n is the refractive index on passing from one ferromagnetic region to another with anti-parallel polarization and R is the length of the neutron path through the domain. Thus the two above mentioned limiting cases are identified as

refraction case: $\varphi \gg 1$
diffraction case: $\varphi \ll 1$

The refractive index on passing from vacuum to a ferromagnetic region can in general be given by

$$n = 1 - 2\pi k^{-2}\left[\sum_i N_i(b_i \pm p_i)\right] \qquad (5.2)$$

where k, as usual, is the neutron wave vector, Ni is the density of atoms of the element i, and b_i and p_i are the coherent nuclear and magnetic scattering lengths respectively of this element. The "$(\pm)$" sign in front of p_i indicates that the refractive index depends on the polarization of the neutron relative to the polarization of the refractive medium.

Total reflection at the boundary will occur if $n<1$ and the angle of incidence (the angle between the wave vector and the boundary surface) is smaller than

$$\varphi_c = \sqrt{4\pi k^{-2}\sum_i Ni(b_i \pm p_i)} \qquad (5.3)$$

Now the refractive index on passing from one ferromagnetic region to another with antiparallel polarization can be calculated as

$$n_{\uparrow\downarrow} = 1 \pm 4\pi k^{-2} \sum N_i p_i \qquad (5.4)$$

and the critical angle for n<1 as

$$\theta_c = \sqrt{8\pi\ k^{-2}\ \Sigma N_i p_i} \qquad (5.5)$$

The numerical values for $LiTbF_4$ can be inserted yielding the following results ($k = 1.55\text{Å}^{-1} \sim E = 5$ meV)

$$n_{\uparrow\downarrow}\ 1 \pm 1.9\cdot10^{-6}\cdot\mu \qquad (5.6)$$

$$\theta_c = \sqrt{3.8\cdot10^{-6}\cdot\mu} \qquad (5.7)$$

where μ is the magnetic moment of the Tb ions in unit of μ_B. As quoted earlier the saturation moment of the Tb^{3+}-ions is 8.9 μ_B and

$$n^{sat}_{\uparrow\downarrow} = 1 \pm 1.70\cdot10^{-5} \qquad (5.8)$$

$$\theta^{sat}_c = 20' \qquad (5.9)$$

Since the size of the domain is not known the phase difference ϕ in eq. 5.1 cannot be calculated. Another calculation can, however, be performed, namely the calculation of the domain size for which $\phi = 1$:

$$R = \tfrac{1}{2}k^{-1}\ (1-n)^{-1} \qquad (5.10)$$

At very low temperatures where the Tb^{3+} ions are saturated $R = 2.0$ µm. But $\lim n\ (T\to T_c) = 1$ and thus $\lim R\ (T\to T_c) = \infty$. The domain size is vanishing at $T = T_c$ and attains its maximum value at T = 0 K. The maximum size can be expected to be larger than 4.4 µm. This analysis shows that

- at T = 0 K refraction is the dominating scattering mechanism
- if T is very close to T_D diffraction is the dominating scattering mechanism
- the experiments presented in this work are performed in a temperature region where the neutron scattering cannot be viewed as belonging purely to one of the limiting cases but must be subject to a more careful analysis.

5.3. Domain refraction

To be able to calculate the neutron scattering due to refraction a domain structure has to be assumed.

The domain structure of magnetically uniaxial crystals has been studied in detail by several authors (see below). The structure was studied in plate-shaped samples, whose planes are perpendicular to the axis of easy magnetization i.e. like the sample in this study.

The domain structure in very thin samples (thickness < 25μ) is well-known. A simple stratified structure of plane-parallel domains is observed in a microscope and theoretical calculations have been carried out by Kittel (1949).

For thicker samples (25-200μ) a more complicated structure is observed in the microscope. Additional domains forming a wavy pattern are found at the surface of the sample and forming spikes into the sample, see fig. 5.4. The theory for this domain structure was developed by Kandanrove and Beketov (1974).

In thicker samples than the one used in this study a more complex structure is expected. It is plausible to assume a structure where the spikes from the structure in the thinner samples are retained but additional spikes are formed in the interior of the sample (Kandanrove and Beketov, 1974).

It is obvious that it is very difficult to make an analytical calculation of the refraction of a divergent neutron beam by a domain structure with the above mentioned complexity. One can, however, manage to keep track of a single neutron as it passes through the sample. Thus it is attractive to estimate the neutron scattering by performing a Monte Carlo calculation (Møllenbach 1975) and this approach was used in the following way. The sample is only studied in the scattering plane. In this plane the sample is divided into plane-parallel sections with a simple spike-structure as shown in fig. 5.5a.

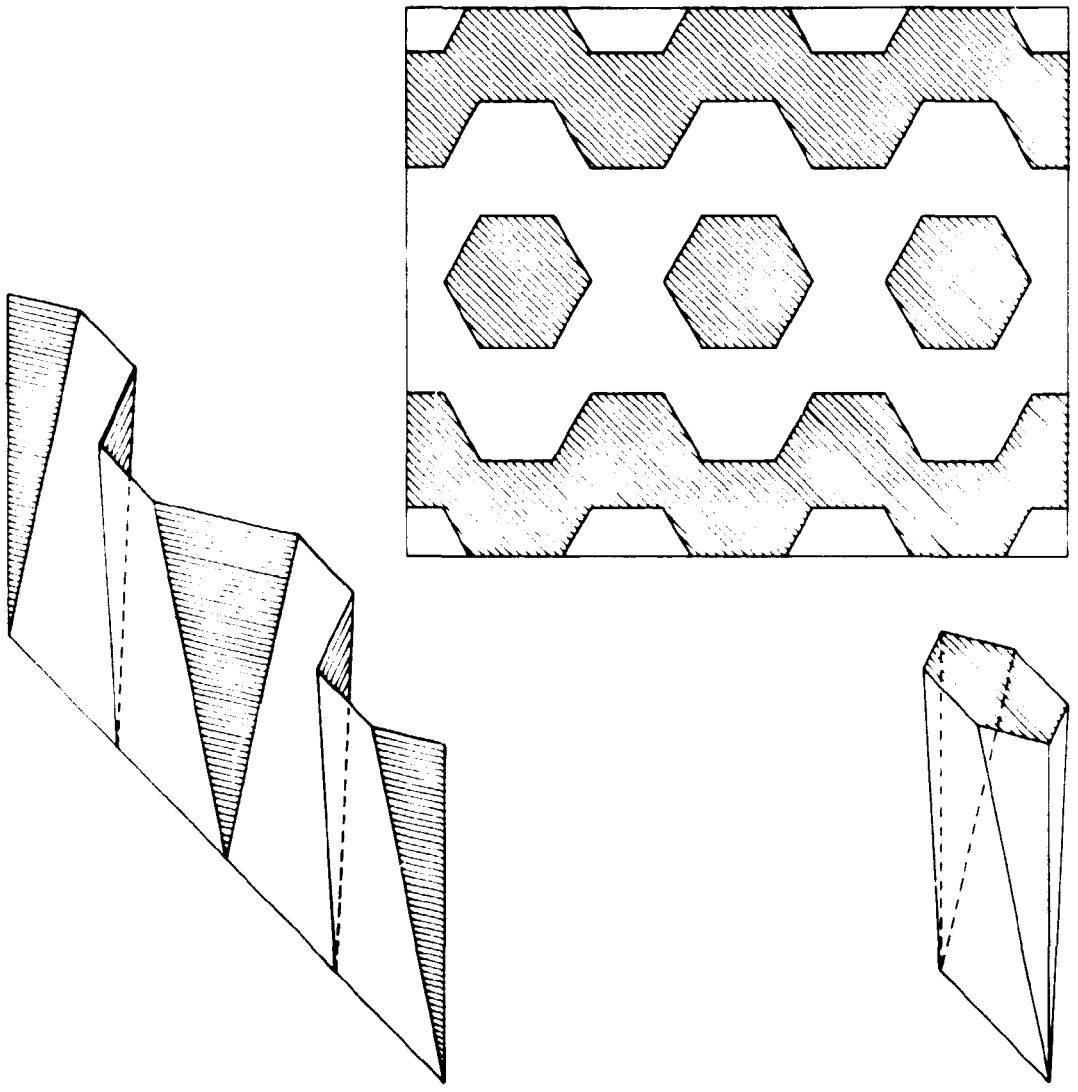

Fig. 5.4. The domain structure studied by Kandanrove and Beketov (1974).

In this sketch w is the width of a spike and d the thickness of the plane-parallel section. This structure is similar to the structure in samples of medium thickness. The more complicated structure for the thick samples is obtained by stacking these sections as shown in fig. 5.5b.

The calculation of neutron refraction is very sensitive to the position and orientation of the domain walls since the domain

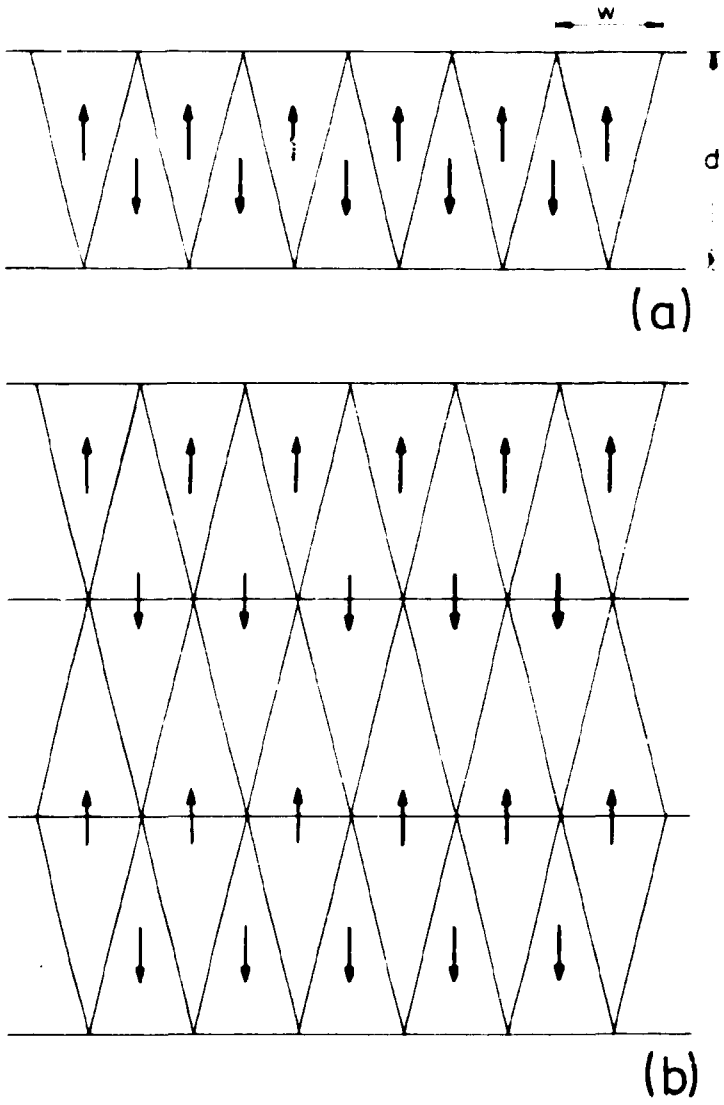

Fig. 5.5. The domain structure used for Monte Carlo calculations. a) a single section with a simple spike-structure. b) 3 sections.

walls are the locations where the computations allow the neutrons to interact with the sample. In this respect the proposed domain model is simplified to a level where the calculated results cannot be expected to yield more qualitative information in relation to the experients.

The calculations gave the following general results:

- with one spike layer the neutron refraction increased as w/d decreased until w/d approached the critical angle for total refraction
- when the number of layers were increased multiple-refraction effects were observed in the form of a primary beam depletion
- although the refraction depends on an intimate interplay between w/d, the number of layers and the neutron beam divergence, all calculations showed vanishing refraction effects for q in the order of $.01Å^{-1}$. Thus neutron scattering observed for $q > .02Å^{-1}$ must be due to other effects than neutron refraction.

All these results are in qualitative accordance with the experimental observations shown in fig. 5.3.

5.4. Domain diffraction

A discussion of the neutron diffraction by the magnetic domain must be based on an assumed domain structure as well as the discussion of neutron refraction was.

The structure used for the Monte-Carlo calculations in the last section is slightly modified to allow for analytical calculations. The domains are assumed to be elongated ellipsoids with the axis of revolution parallel with the Ising axis. The ellipsoids are distributed so that along any line perpendicular to the Ising axis one will find a collection of domains with alternating polarization and the length of the path through a domain is given by a normal distribution with mean value κ^{-1} or in other works κ^{-1} is the average domain width perpendicular to the Ising axis. Along the Ising axis one will find a similar distribution but in this direction the average domain width is $c \cdot \kappa^{-1}$.

Apart from being a plausible model based on observations in thin samples this model is a simple three dimensional extension of the one dimensional random domain model proposed by Cowley et al. [5.7].

The calculation of the spin-spin correlation function is found in detail in appendix C and yield the following result for its Fourier transform.

$$S(\vec{q}) = \left(\frac{M}{M_0}\right)^2 \cdot \frac{\cdot}{(\cdot^2 + q_x^2 + q_y^2 + c^2 q_z^2)^2} \tag{5.11}$$

This result assumes an infinitesimal thickness of the domain boundaries. A finite thickness of these will enter the scattering cross-section as an effective form factor and

$$\left(\frac{d\cdot}{d\cdot}\right)_{\text{domain}} = S(q) \cdot F(q) . \tag{5.12}$$

If the domain wall is shaped like an exponential function and the domain wall width, $\cdot$, is the 1/e-width then the formfactor is

$$F(q) = \frac{1}{1 + (\cdot \cdot q)^2} \tag{5.13}$$

The total cross-section for domain diffraction then has the form

$$\left(\frac{d\cdot}{d\cdot}\right)_{\text{domain}} = \left(\frac{M}{M_0}\right)^2 \frac{\cdot}{(\cdot^2 + q_x^2 + q_y^2 + c^2 q_z^2)^2} \cdot \frac{1}{1 + (\cdot q)^2} \tag{5.14}$$

5.5. Analysis of the domain diffraction data

As discussed in section 5.3 only the data from region 1 with $.02 < q_x < .06$ can be analyzed as originating from domain diffraction. Since κ^{-1} has an order of magnitude of several μm then $\cdot \ll q_x$ and the cross-section reduces to

$$\left(\frac{d\sigma}{d\Omega}\right)_{\text{domain}} \propto \left(\frac{M}{M_o}\right)^2 \cdot \frac{\kappa}{(q_x^2 + q_y^2 + c^2 q_z^2)^2} \cdot F(q) \qquad (5.15)$$

or

$$\left(\frac{d\sigma}{d\Omega}\right)_{\text{domain}} \propto \left(\frac{T_c - T}{T_c}\right) \frac{\kappa}{(q_x^2 + q_y^2 + c^2 q_z^2)^2} \cdot F(q) \qquad (5.16)$$

where the known temperature dependence (neglecting the small logarithmic corrections) of the magnetization has been used.

It is clear from this formula that the absolute value of κ cannot be found in this analysis. This would be the case if it had been possible to separate the domain diffraction from the domain refraction in region 2 i.e. find data for $q_x \sim \kappa$.

Measurements of the domain diffraction were made for $q_z = q_y = 0$. These measurements were made with a rather coarse vertical resolution. This is accounted for in a crude manner using the fact that the cross-section is isotropic in the (q_x, q_y)-plane. The q_x is then simply replaced by an effective $q_{x,eff.}$ defined by

$$q_{x,eff.}^2 = \frac{1}{\sigma_y} \int_0^{\sigma_y} (q_x^2 + q_y^2)\, dq_y = (q_x + \frac{1}{3}\sigma_y^2) \qquad (5.17)$$

where σ_y is the half width at half maximum of the vertical resolution. Including this effective q_x leeds to the following equation for the intensity

$$I(q_x,0,0) \propto k' \cdot \frac{1}{q_{x,eff.}^4} F(\lambda \cdot q) \qquad (5.18)$$

where k' and λ are parameters with a possible temperature dependence.

The temperature dependence of λ, the domain wall width, were studied theoretically by Kent Joel (1976). In his work a simple mean field argument leeds to the conclusion that

$$\lambda \propto t^{-\frac{1}{2}}, \quad t = 1 - \frac{T}{T_c} \tag{5.19}$$

Adopting this result and assuming that κ will follow a powerlaw as T approaches T_c it should be possible according to eq. 5.18 by a suitable scaling of the data to plot these on one curve which is the effective form factor or the Fourier transform of the domain wall.

This is indeed possible with data obtained if κ has the temperature dependence

$$\kappa \propto t^{-\frac{1}{2}} \tag{5.20}$$

as $T \to T_c$. The plot is seen in fig. 5.6 where $I \cdot q_{eff.}^{4}/\sqrt{t}$ is plotted versus $a \cdot q/\sqrt{t}$. (a is the length of the unit cell along the x-direction).

The solid curve is a plot of the form factor obtained from fitting eq. 5.13 to the data. This yields

$$\lambda = 5.2 \cdot t^{-\frac{1}{2}} \text{ Å} \tag{5.21}$$

One more parameter in the cross-section, eq. 5.14, can be determined from the experiments: the anisotropy constant c.

If the domain wall widths in the directions close to the Ising axis are of the same order of magnitude as in the perpendicular direction and if $c >> 1$ then the magnitude of the form factor will be given by q_x in a q_z-scan. In other words: for a fixed temperature and fixed q_x the intensity in a q_z-scan is given by

$$I = \text{const.} \frac{1}{(q_x^2 + c^2 q_z^2)^2} \tag{5.22}$$

and the half width at half maximum is then

$$q_z^{HWHM} = q_x \frac{\sqrt{\sqrt{2}-1}}{c} \tag{5.23}$$

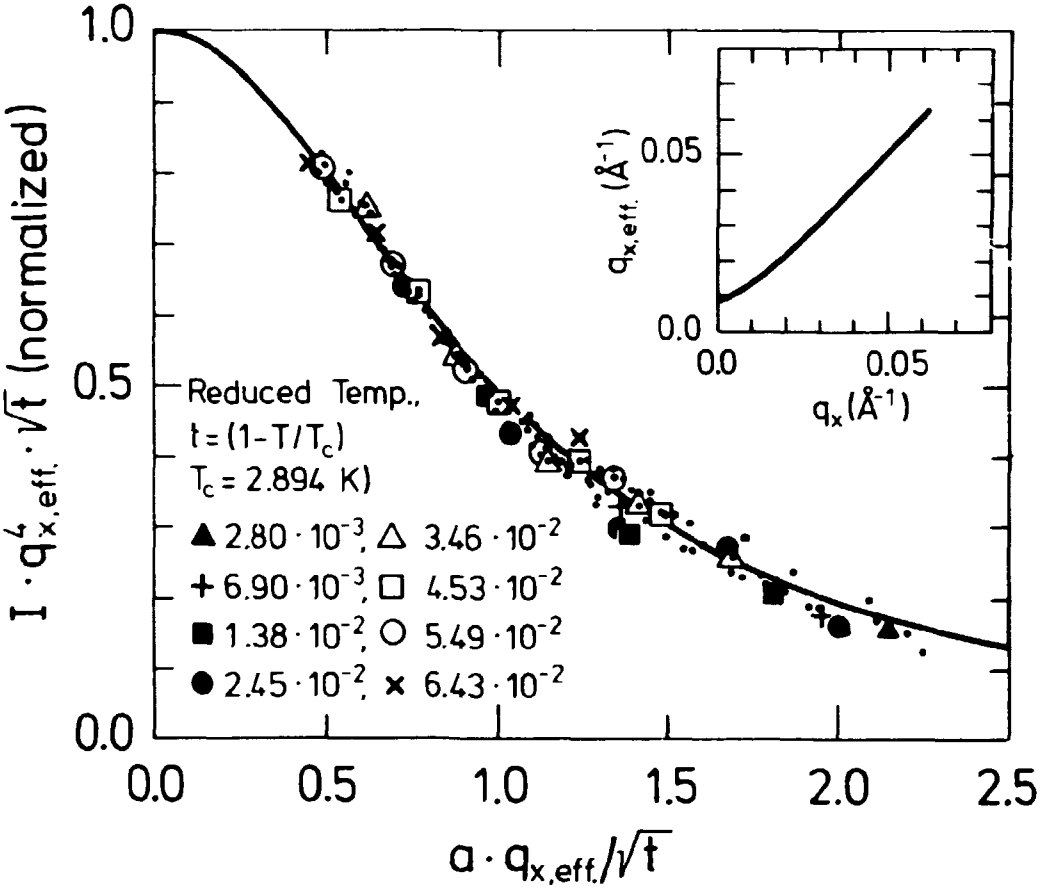

Fig. 5.6. The domain wall formfactor in $LiTbF_4$. It is shown that the experiments support the theory developed in sections 5.4 and 5.5 since a domain wall formfactor results from plotting $I \cdot q_{x,eff.}^4 \cdot \sqrt{t}$ versus $a \cdot q_{x,eff.}/\sqrt{t}$. The insert gives the relation between q_x and $q_{x,eff.}$ equivalent to eq. 5.17.

Thus for a fixed temperature the cross-section in equation (5.22) indicates that q_x plotted versus q_z^{HWHM} is a straight line and c is found from the slope of this line.

This plot is seen in fig. 5.7 and the linear dependence is verified. Data were obtained at five different temperatures in the interval $10^{-2} < t < 1.5 \cdot 10^{-1}$ and it was observed for a given q_x that q_z^{HWHM} is constant. Thus c is temperature independent and from the plot is found that

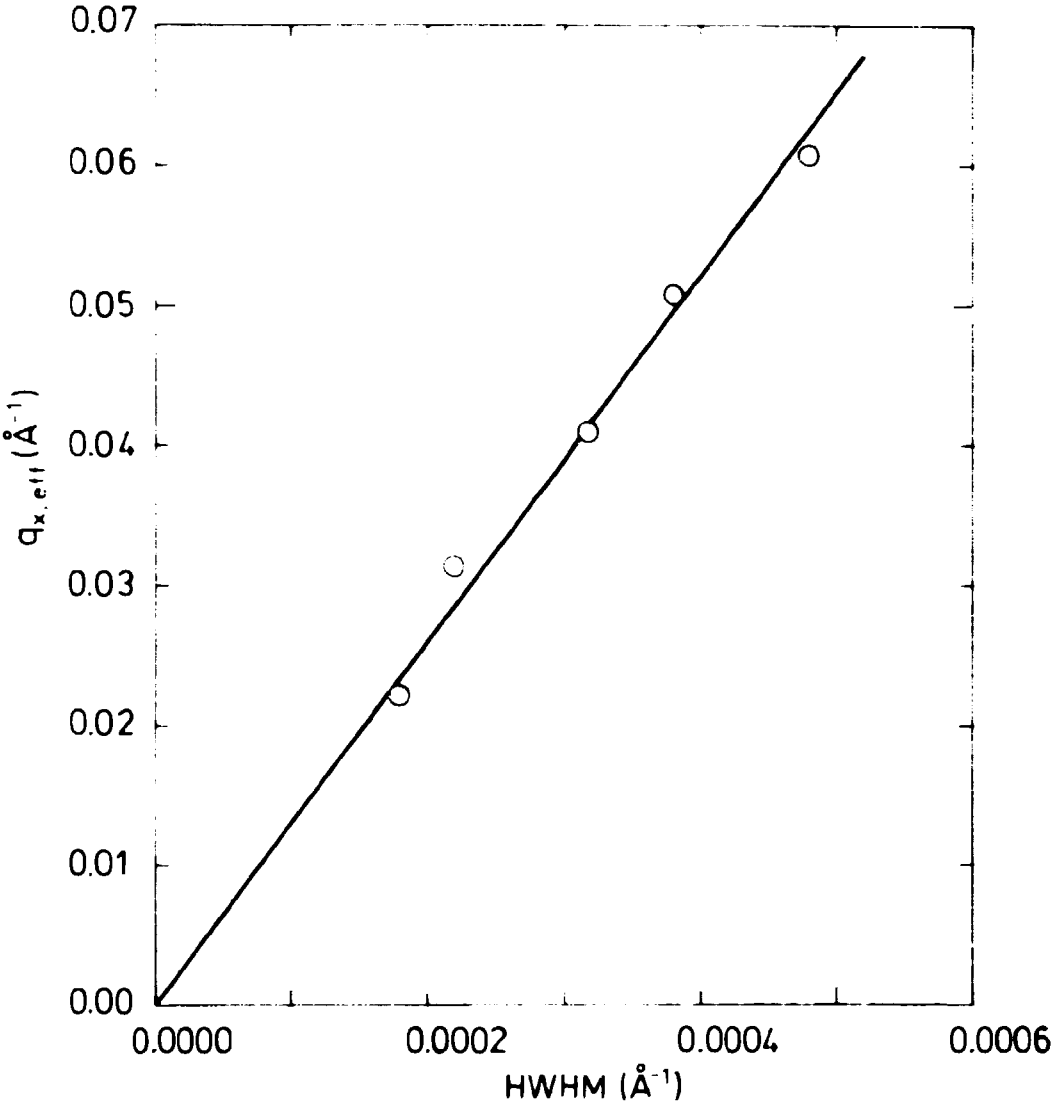

Fig. 5.7. The domain anisotropy. The plot shows the half width at half maximum (HWHM) in a q_z-scan for fixed q_x-values. Each point represents measurements at 5 different temperatures. HWHM is temperature independent and so is the anisotropy constant, c, which can be calculated from the slope of the line as seen in eq. 5.23.

$$c = 84 \qquad (5.24)$$

The results of the analysis can be summed up as follows:

The domain diffraction data measured in the region .02 $Å^{-1}$ $< q_x <$ .06 $Å^{-1}$ are well described by the cross-section

$$\left(\frac{d\sigma}{d\Omega}\right)_{\text{domain}} \propto \left(\frac{M}{M_o}\right)^2 \frac{\kappa}{(\kappa^2 + q_x^2 + q_y^2 + c^2 q_z^2)^2} \cdot \frac{1}{1 + (\lambda \cdot q)^2} \,. \tag{5.25}$$

With the assumptions

$$\lambda \propto t^{-\frac{1}{2}} \tag{5.26}$$

and

$$\kappa << q_x$$

the data shows

- for the inverse domain width

$$\kappa \propto t^{-\frac{1}{2}} \tag{5.27}$$

- for the domain wall width.

$$\lambda = 5.2 \cdot t^{-\frac{1}{2}} \text{ Å} \tag{5.28}$$

and

- for the anisotropy constant

$$c = 84. \tag{5.29}$$

5.6. Summary

Neutron scattering is observed at very small angles below the Curie temperature in the Ising ferromagnet $LiTbF_4$.

The neutron scattering has two contributions:

At very low angles neutron optical effects are responsible for the neutron scattering. The most spectacular feature, an almost complete depletion of the primary beam, of this contribution as well as its extension in reciprocal space can be qualitatively understood from Monte-Carlo calculations with a simple domain model.

The second contribution is domain diffraction observed beyond the limits of the domain refraction i.e. for $q_x > .02\text{Å}^{-1}$. It is possible to calculated a neutron scattering cross-section from a simple but plausible domain model where the domains are assumed to be shaped like ellipsoids along the Ising axis and where the scattering depends on three parameters: κ, the domain width in the direction perpendicular to the Ising axis, λ, the domain wall width and, c, the anisotropy of the domains i.e. the ratio between the domain width in the directions parallel to and perpendicular to the Ising axis. From analysis of the experimental data it has been possible to find the absolute value of λ and c, the temperature dependence of λ and κ and the lack of temperature dependence of c. The results have been summed up in section 5.5.

These findings suggest that the formation of domain in a ferromagnet is coupled to the thermodynamics of the system. Conclusive evidence for this statement is not found in the experimental data presented here. Only experiments with other systems and experimental methods where only one scattering mechanism is present can reject or prove the model proposed in this work.

6. SMALL ANGLE NEUTRON SCATTERING FROM PROTEINS AND PROTEIN-COMPLEXES IN AQUEOUS SOLUTIONS

Structures of molecular biological systems are commonly studied with an electron microscope. This instrument is, however, limited to give information on a scale down to typically 100Å. If one wants to study details in biological systems with linear dimensions smaller than this limit other methods must be used. Neutron- and X-ray scattering are possible methods and have in recent years been tested as tools in several studies in molecular biology. While X-rays are advantageous to use from the point of view of intensity and cost of equipment, neutrons are attractive due to one unique physical property. There is a large difference in the coherent neutron scattering length of hydrogen and deuterium, thus one can label or "stain" a sample or parts of it by a suitable exchange of hydrogen with deuterium.

The interest from molecular biologists has been concentrated around three groups of compounds.

These are

1) Protein single crystals
2) Well-oriented molecular biological systems
3) Macromolecules (e.g. proteins and protein-complexes) in aqueous solution.

Single crystals can be grown from a number of proteins. Thus detailed information on an atomic level can be obtained from diffraction experiments. When the hydrogens are exchanged with deuteriums neutron diffraction allows not only for the determination of the positions of the heavier atoms but also the determination of the hydrogen (deuterium) positions. An example illustrating the work with protein crystals is the study by Norwell and Schoenborn (1976) of the myoglobin and hemoglobin.

The second group of compounds consists of a limited number of molecular biological systems built from well-oriented organic units and are thus almost crystalline in one or more directions. A very interesting example in this group is the lipid bilayer membrane which is the most common barrier in biological systems. This structure resembels the smectic phase of liquid crystals. The main goal in studying these systems is to find how proteins responsible either for transport of other molecules through a membrane or for recognition of certain stimuli are embodied in the membrane. An illustrative example of this work is the study of retina membranes by Yeager (1976).

Finally a number of macromolecules are studied in aqueous solutions. Often one can isolate a protein complex for which the structural conformation is of interest for its biological function. Through biochemistry the protein components can be separated and identified but information on their relative positions in the complex is lost and with that a detailed understanding of the function of the complex. Diffraction studies can give the structural information.

While the diffraction studies of the compounds in the first two groups can be done with "conventional" diffractometers then the study of macromolecules in solution is a task for a small angle scattering instrument, the SAS, and a discussion of this field of research is the subject of this chapter.

The general principles are illustrated through a discussion centered around a specific example: the study of histones and histone-complexes by neutron scattering. This study is in progress in the Department of Biology of the Brookhaven National Laboratory, U.S.A. This example is chosen despite the fact that it is to early to present actual result since the author had the oportunity of participating in some of the preliminary experiments, and the illustrations have to be principle sketches taken from other studies.

6.1. Histones

It is well known that the genetic information in cells in higher organisms is found in particles in the cell-core called chromosomes. The chromosome-material or chromatin consists of a long (approximately 2 m) DNA-molecule neatly coiled and a number of small proteins. Five of these have special interest, they are called the histones. The reason for the special interest is firstly the fact that they are conserved i.e. identical in all higher organisms and secondly because they are believed to play an important but yet not fully known role for the structure of the chromatin.

If the chromatin is strehched a bead structure is observed in an electron microscope as well as through X-ray and neutron scattering studies (Bradbury et al, 1976). The beads are called nucleosomes or ν-bodies, and they consist of a core particle surrounded by the DNA molecules. The core particle is a double tetramer of four of the histones, $(H2a, H2b, H3, H4)_2$. The fifth histone, H1, is attached to the DNA between the ν-bodies. The individual histones are very well characterized from biochemical analysis (De Lange et al, 1975) like other proteins they are coiled and they are spherical but with their ends ionized and streching out of the sphere like arms. It is believed that the globular parts are responsible for histone-histone bindings while the arms are responsible for histone-DNA-bindings.

To find the role the histones for the structure of the chromatin it is of interest to study the detailed structure of the nucleosome core particle i.e. the $(H2a, H2b, H3, H4)_2$-complex.

6.2. The strategy of the studies

The study of the conformation of the ν-body core-particle has two parts. The most lengthy and complicated part is the biochemical work involved in the sample preparation. Not only must the procedures used for separating the eight proteins be

mastered but new methods must be developed firstly to produce deuterated histones and secondly to reconstruct the double-tetramer complex from its individual components either in hydrogenated or deuterated form.

The easy part of the study is the neutron-scattering experiment. On one hand the measurements are few and rather fast, and the interpretation straight forward. On the other hand the strategy in the study is set by the scattering experiment and thus the demands the development of the procedures necessary for a specific sample preparation.

The scattering experiments have two main stages. The first stage is to characterize the scattering properties of the pure individual components of the protein-complex i.e. to find the average scattering length density of each of the histones H2a, H2b, H3 and H4 in hydrogenated as well as deuterated from.

The second stage is to study the scattering from the reconstructed histone-complex with one or two histones deuterated and the other seven or six hydrogenated (or vice-versa). From these measurements the distances between all histone pairs can be found and through a triangulation procedure the conformation of the histone-complex can be determined.

In between these two main stages several substages are found. The step from the study of the individual histones to the total histone-complex is too difficult so smaller steps are taken by studying smaller histone complexes: dimers and tetramers.

6.3. Measurements of the radius of gyration and the match point

The scattering properties of a protein-molecule is described by the scattering length density defined in sec. 2.1, $\rho(\bar{r})$, and the scattering properties of an aqueous solution of proteins are given by $\rho_{solute}(\bar{r})$. They are equated as

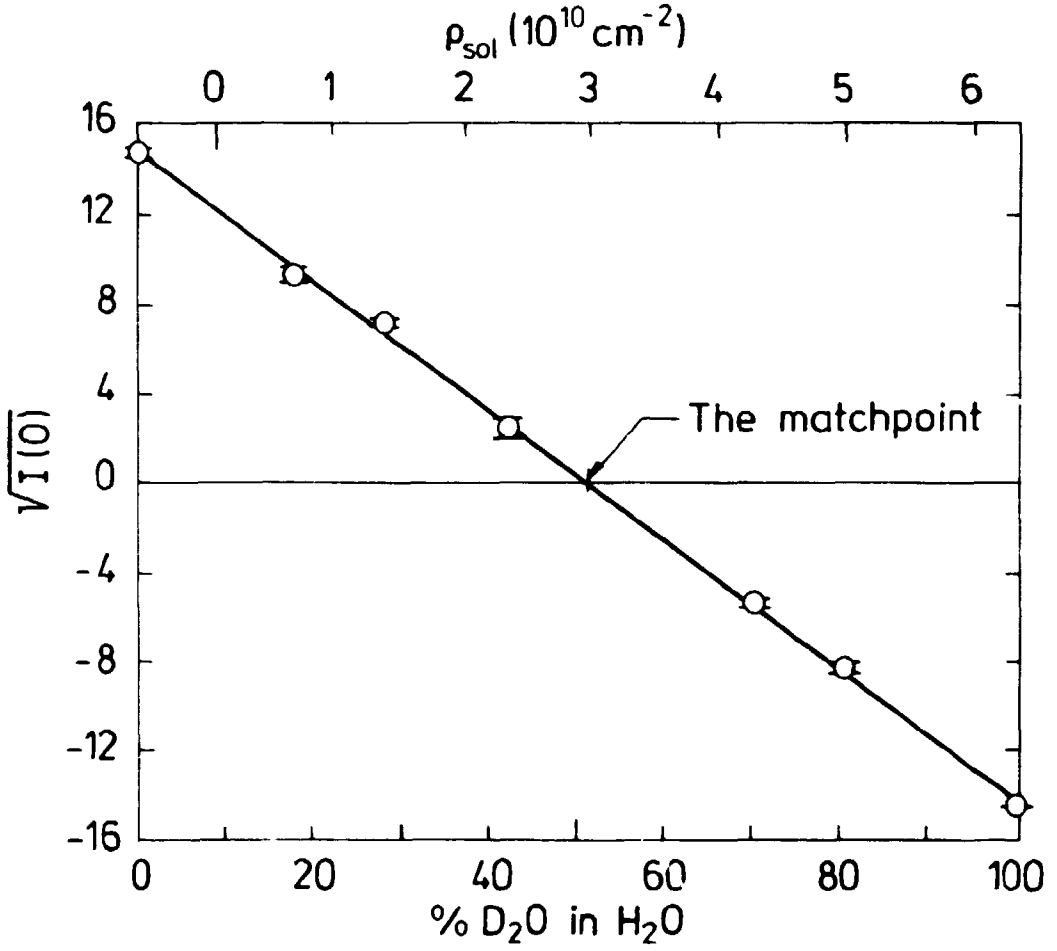

Fig. 6.1. Contrast dependence of the zero angle scattering. From this plot the matchpoint is identified. Experiments by R.P. Hjelm et al. (1977) with ν-bodies in water.

$$\rho(\bar{r}) = \rho_{solute}(\bar{r}) - \rho_{solvent}(\bar{r}) \tag{6.1}$$

or

$$\rho(\bar{r}) = \rho_{solute}(\bar{r}) - \bar{\rho}_{solvent} \tag{6.2}$$

where $\rho_{solvent}(\bar{r}) \equiv \bar{\rho}_{solvent}$ is the scattering length density of the homogenious solvent. For the mean values one has

$$\bar{\rho} = \bar{\rho}_{solute} - \bar{\rho}_{solvent} \tag{6.3}$$

$\bar{\rho}$ is also called the contrast. $\bar{\rho}_{solvent}$ depends on the composition of the solvent i.e. on the H_2O/D_2O-ration since only proteins in aqueous solutions are considered here. For all proteins (and all major molecules in biological systems) the change of value of $\bar{\rho}_{solvent}$ upon exchange of H_2O with D_2O will change the sign of $\bar{\rho}$ from positive to negative. The H_2O/D_2O ratio at which the contrast is zero is called the match point.

The radius of gyration is defined as the square root of the second moment of the scattering length density distribution within the particle and is dependent on the size and shape of the particle and the contrast. Thus the equation defining the radius of gyration is

$$R = \left(\int_{part.} \rho(\bar{r}) \cdot \bar{r}^2 \cdot d\bar{r} / \int_{part.} \rho(\bar{r}) \cdot d\bar{r} \right)^{\frac{1}{2}} \qquad (6.4)$$

The neutron-scattering cross-section and hereby the intensity can as described in section 2.1 be calculated from the scattering length density distribution.

The matchpoint can be found from the intensity at zero scattering-angle since this intensity is given by

$$I(o)/c = \text{constant} \cdot \bar{\rho}^2 \cdot v^2 \cdot M/N \qquad (6.5)$$

in terms of the concentration of proteins c, molecular weight M, partial specific volume v and Avogadro's number N.

Guinier (1955) has shown that close to the forward direction the intensity of the neutrons scattered from a dilute solution of randomly oriented molecules can be described by a Gaussian function

$$I(q) = I(o) \exp\left[-q^2 \cdot R^2/3\right] \qquad (6.6)$$

Thus a plot of the logarithm of the intensity versus the squared momentum transfer (known as a Guinier-plot) should be linear as the momentum transfer approaches zero and the radius of gyration is given by the square root of the slope of the line.

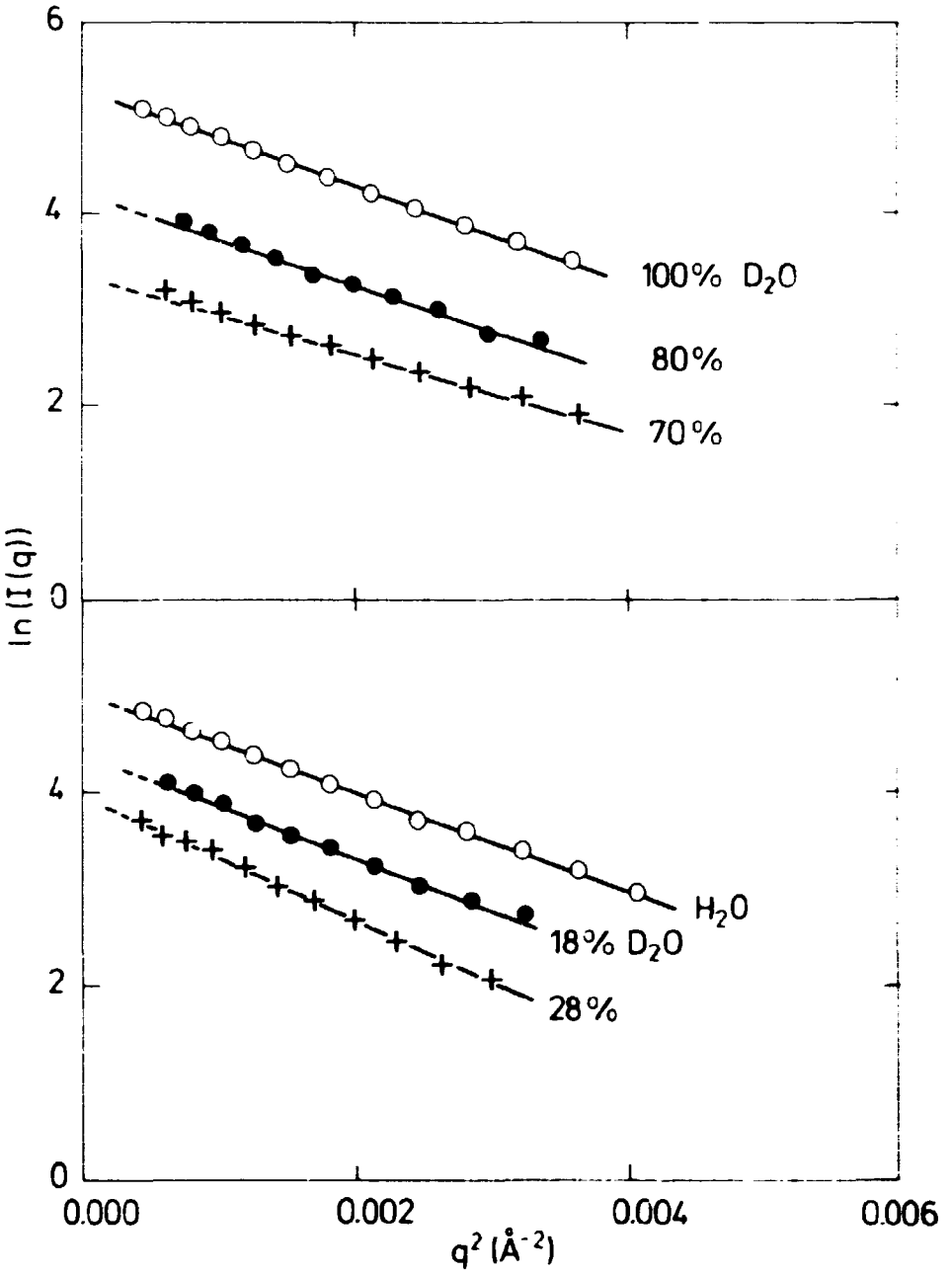

Fig. 6.2. Guinier plots. The experimental points for each contrast fit to a linear relationship and the slope of each plot is proportional to the radius of fyration - see eq. 6.6. Experiments with ν-bodies in water by R.P. Hjelm et al. (1977).

As mentioned above the radius of gyration depends on the contrast. This has been studied in more detail by Stuhrmann (1976). He has shown that the measured radius of gyration can be expanded in the inverse contrast as

$$R = R_T + \alpha \frac{1}{\bar{\rho}} + \beta \frac{1}{\bar{\rho}^2} \qquad (6.7)$$

where R_T is the true radius of gyration or the radius of gyration measured when the particle is in infinitely high contrast. The coefficients α and β, describes the deviations of $\rho(\bar{r})$ from $\bar{\rho}$ found in the interior of the protein for instance due to penetration of the solvent into the protein.*

The details of the neutron scattering experiment and its interpretation are as follows: For each measurement of an intensity-profile I(q) at a given sample concentration and a given contrast four sample cuvettes are prepared. These are

A) An empty cuvette
B) A cuvette with a purely incoherent scattering sample (8% D_2O in H_2O)
C) A cuvette with the protein solution

and

D) A cuvette with the pure solvent.

With all the samples the transmitted primary beam is measured as well as the small angle scattering when the transmitted primary beam is caught in a beam stop before the detector.

---

*Stuhrmann (1976) has also in detail studied effects of H-D exchange from solvent to protein and of deviations from spherical shape of the protein. The H-D exchange is neglected in the present discussion. So is the effect from a possible non-spherical shape of the proteins since they are studied at momentum transfers outside the Guinier-region where the intensity is very low and it is dubious whether statistics for a proper interpretation of these data can be obtained.

The transmitted intensities are called t_i, i = A,B,C,D. The small angle scattering $I_i(q)$, i = A,B,C,D. Note that this scattering is only a function of the absolute value of the momentum transfer since the samples are isotropic solutions. The small angle scattering from the samples A, C and D are scaled by the small angle scattering from sample B to correct the data for inhomogenities in the detector system, to give the corrected intensities I^C as

$$I_i^C(q) = I_i(q) \cdot I_B(q) \qquad i = A,C.D. \qquad (6.8)$$

Now the scattering from the proteins is calculated as

$$I_{protein}(q) = \left(\frac{I_C^C(q)}{t_C} - \frac{I_A^C(q)}{t_A}\right) - f \cdot \left(\frac{I_D^C(q)}{t_D} - \frac{I_A^C(q)}{t_A}\right) \qquad (6.9)$$

where f is the volume fraction of solvent in the solution containing the solute.

First a series of measurements is made to check the concentration dependence given in eq. 6.5. One would like to have a high concentration of proteins in the solute in order to have a high protein signal, but the concentration should still be far below the limit where protein-protein correlations affect the scattering and eq. 6.5 breaks down. Typical values for concentration are 5-20 mg/ml for a large number of proteins.

After a reasonable protein concentration has been found a series of measurements is made with varying H_2O/D_2O-ratio in the solvent. These data are processed with eq. 6.9 and Guinier-plots are made. Typical examples for varying contrast are seen in fig. 6.2. From the curves in the Guinier-plot two parameter sets are extracted.

Firstly the extrapolated values of the intensity at zero momentum transfer are collected and plotted versus the H_2O/D_2O-ratio, see fig. 6.1. This plot gives the match-point and thus sets the scale for $\bar{\rho}$. Secondly the radii of gyration are found from the curves in the Guinier-plot and plotted versus $1/\bar{\rho}$, see fig. 6.3. This plot gives the "true" radius of gyration.

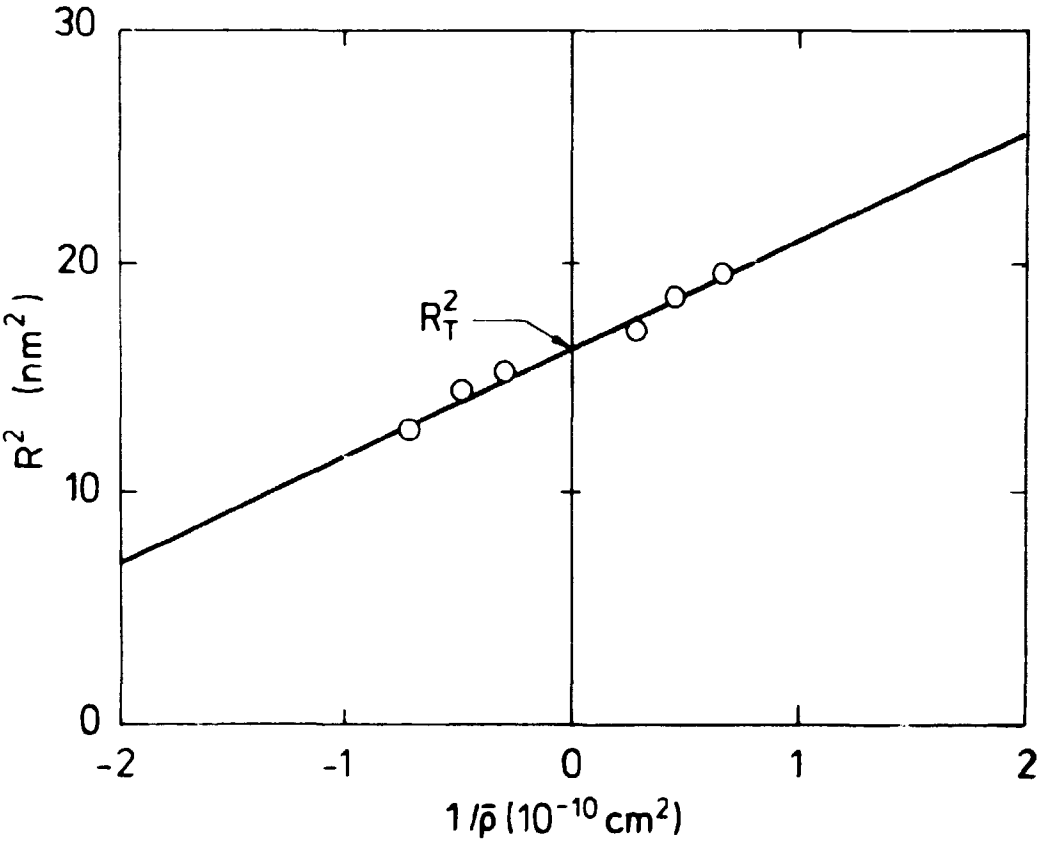

Fig. 6.3. Contrast variation of the radius of gyration. From this plot the true radius of gyration can be found. Experiments by R.P. Hjelm et al. (1977).

This completes the procedure for finding the most important parameters characterizing the scattering properties of a protein in an aqueous solution.

6.4. Triangulation technique

When the scattering properties of the individual components in a protein-complex have been determined one can turn to the measurements determining the distances between all pairs of components in the complex.

Let two components, I and II, be chosen. To enable the measurement of the distance between these two the protein-complex must be produced in four forms representing all the combinations of the components I and II in either hydrogenated or deuterated form. The scattering amplitudes for these samples are given by

$$A_{complex,i,j} = A_{I,i} + A_{II,j} + A_{rest.} \tag{6.10}$$

where $\left.\begin{matrix} i \\ j \end{matrix}\right\}$ = H or D.

The scattering intensity is given by

$$I_{ij} = |A_{complex,i,j}|^2 \tag{6.11}$$

It is easy to show that a combination of the intensities from the four samples, which is only a function of the two components chosen, and independent of the rest of the complex can be made. This combination is illustrated in fig. 6.4 and given by

$$I_{pair} = I_{D,D} + I_{H,H} - I_{D,H} - I_{H,D} \tag{6.12}$$

If the components I and II are spherical they can within the experimental resolution be approximated by points with a distance $R_{I,II}$ between them and

$$I_{pair} \sim \frac{\sin(q \cdot R_{I,II})}{q \cdot R_{I,II}} \tag{6.13}$$

This formula can be fitted to the measured I_{pair} to give $R_{I,II}$.

While it was important in the measurements described in sec. 6.3 to work with a suitably low concentration of the proteins to avoid protein-protein correlations the measurements of I_{pair} can be made at high concentrations since the contributions from complex-complex correlations are averaged out. I_{pair} is also independent of the solvent around the protein-complexes so the proper choice of solvent is that which minimizes the

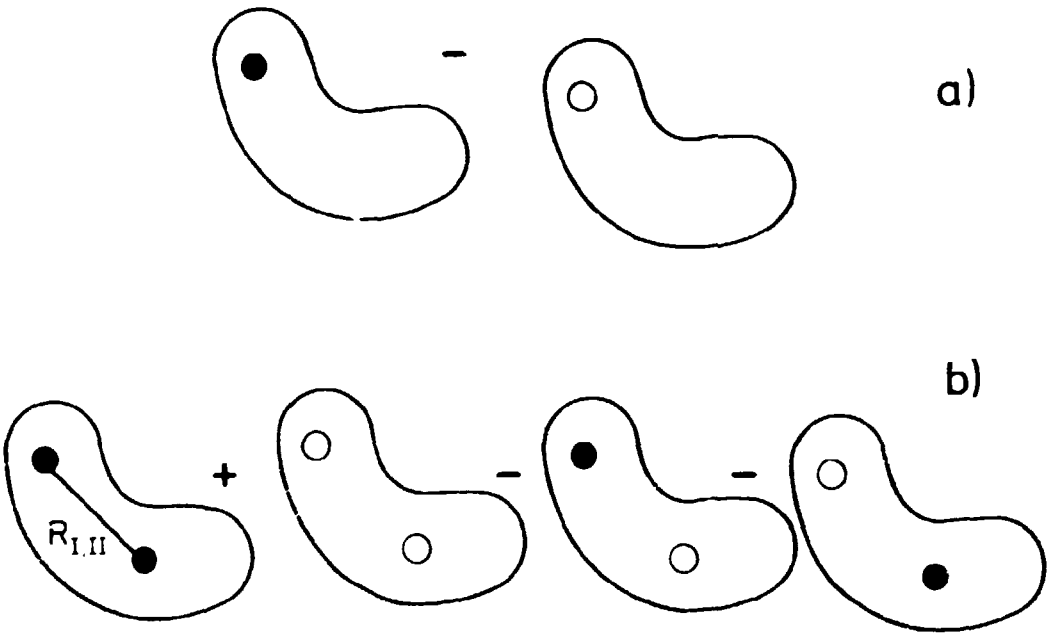

Fig. 6.4. a) represents schematically a complex particle, in which a component can be deuterated (•) or protonated (o). The difference between the scattering of the particle in the two states will give information on that component. b) represents the triangulation method. The measure as shown will give a determination of the distance $R_{I,II}$.

contributions from A_{rest} and thus enhance the signal-to-background ratio.

If the components I and II have for instance an elongated shape eq. 6.13 must be modified. This has been discussed by Hoppe et al. (1976).

Fig. 6.5 illustrates the succesful use of the triangulation method as proved by Engelman et al. (1975), in the study of RNA-subunits, ribosomes.

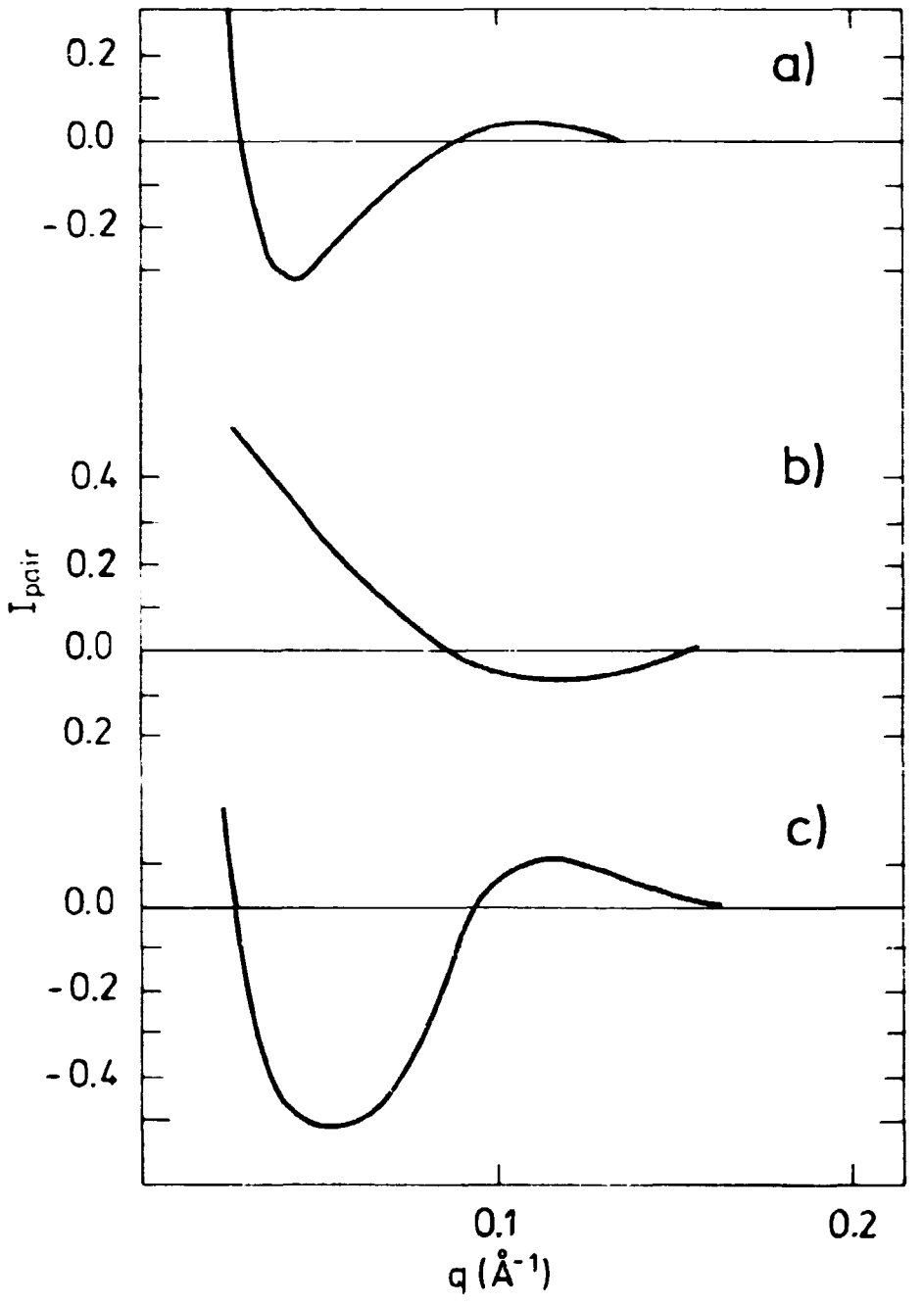

Fig. 6.5. Triangulation experiments on the 30S ribosomal subunit by Engelman et al. (1975). Three examples are given for intensity differences obtained as explained in the text and in fig. 6.4. The following distances are measured a) 105 Å (pair S_2-S_5) b) 35 Å (pair S_5-S_8) and c) 115 Å (pair S_3-S_7).

6.5. Small angle scattering at Risø National Laboratory

The neutron scattering experiments described in the preceding sections can only be made if a very high neutron flux in connection with a very low background is available. The high flux is needed since biological samples in general are small. The low background is a necessity to be able to operate an open geometry instrument (the SAS with the large position sensitive detector) and obtain a reasonable signal-to-background ratio.

These conditions are only fulfilled at very few of the existing research reactors where neutron scattering is performed. It is not surprising that small angle scattering techniques in the first place have been developed at the high flux reactors at the Institute Laue-Langevin (ILL), in Oak Ridge National Laboratory and Brookhaven National Laboratory.

At some medium-flux reactors the described conditions can, however, also be fulfilled. The high flux (at low neutron energies) is obtained by installation of "cold neutron sources" and the low background is obtained by transferring the "cold neutrons" to experimental halls at some distance from the reactor through slightly curved neutron guide tubes. At the research reactor DR 3 of the Risø National Laboratory these installations have been made (J. Als-Nielsen and J.K. Kjems 1975). The experimental hall with the end of the neutron guide tube is shown in fig. 6.6. J. Als-Nielsen and the author performed experiments to show that flux and background were sufficient to support a small angle scattering instrument positioned in the cross-hashed area.

The experimental conditions described by Stuhrmann et al. (1976) were copied and the data shown in table 6.1 were measured. It is seen that the flux measured at DR 3 at equivalent resolution is only about a factor of 3 less than at ILL. In view of the relatively short data collection time at the SAS-instrument this deficit is by no means prohibitive for obtaining data of equivalent quality.

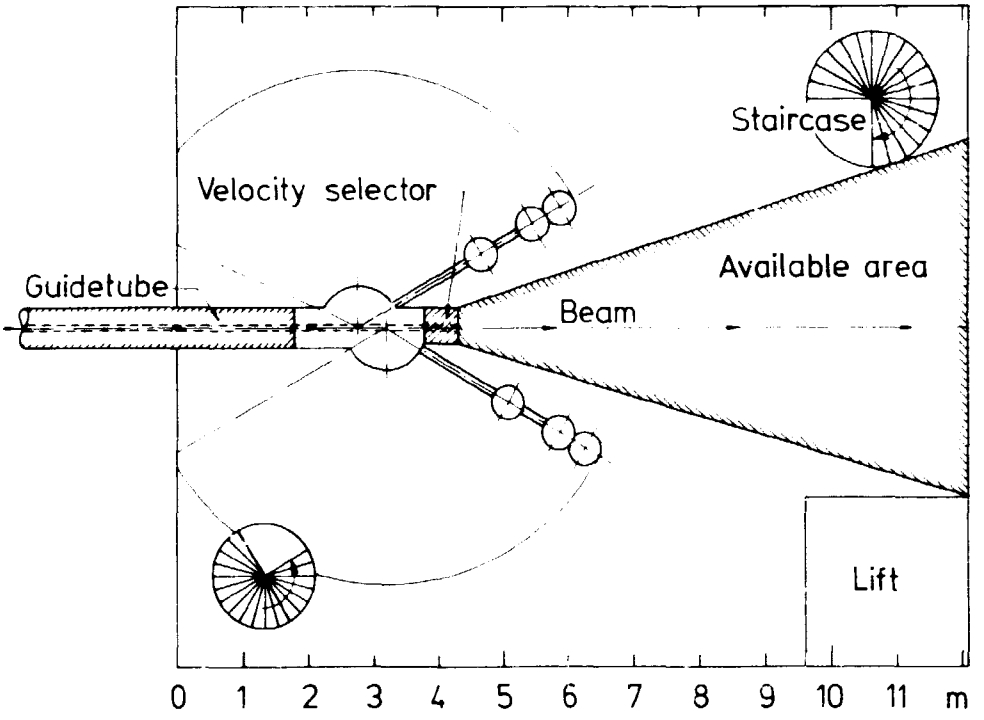

Fig. 6.6. The experimental hall at DR 3. The cross hatched area is a possible site for a SAS instrument.

Table 6.1. Comparison of experimental characteristics of the ILL SAS-instrument (Stuhrmann et al., 1976) and those obtainable at a DR 3 SAS-instrument

	wavelength	wavelength band	neutron flux
	λ Å	$\Delta\lambda$ Å	ϕ $n/cm^2/sec$
RNL	3.4	1.1	1.2×10^7
ILL	3.5	1.5	5×10^7

Thus it is an obvious possibility to make SAS-facility at DR 3 and make small angle scattering experiments possible at a centre in Northern Europe.

ACKNOWLEDGEMENTS

The main part of the work was carried out at the Physics Department of the Risø National Laboratory and the author wishes to express his gratefulness to the members of the neutron scattering group, scientists and technicians, for their never failing assistance and advice throughout the study.

The inspiring guidance from and collaboration with drs. J. Als-Nielsen and J.K. Kjems is gratefully acknowledged.

The final part of the work was carried out at the Biology Department of the Brookhaven National Laboratory, U.S.A. The World Health Organization (WHO) is acknowledged for providing the funding for these studies. The author is very grateful for having experienced the hospitallity of and inspiring collaboration with Dr. B. Schoenborn and his staff.

Dr. H. Bjerrum Møller is thanked for his deep interest in this project.

REFERENCES

AHARONY, A. (1973). Phys. Rev. B8, 3363-3370.

AHLERS, G., KORNBLITT, A. and GUGGENHEIM, H.J. (1975). Phys. Rev. Lett. 34, 1227-1230.

ALS-NIELSEN, J. and KJEMS, J.K. (1975), Risø-M-1862.

ALS-NIELSEN, J. (1976a). Phys. Rev. Lett. 37, 1161-1164.

ALS-NIELSEN, J. (1976b). Phase Transitions and Critical Phenomena (Domb and Green edit) (Academic Press, New York) 5A, 88-165.

ALS-NIELSEN, J., BIRGENEAU, R.J., KAPLAN, M., LISTER, J.D. and SAFINYA, C.R. (1977). Phys. Rev. Lett. 39, 352-355.

ANNUAL REPORT, Oak Ridge National Laboratory (1977).

BACON, G.E. (1975). Neutron diffraction. 3rd ed. (Clarendon Press, London).

BJERRUM MØLLER, H. and NIELSEN, M. (1969). Acta Cryst. A25, 547-550.

BRADBURY, E.M., BALDWIN, J.P., CARPENTER, B.G., HJELM, R.P., HANCOCK, R. and IBEL, K. (1976). Brookhaven Symp. on Neutron Scattering in Biology, IV97-IV117.

COOKE, A.H., MARTIN, D.M. and WELLS, M.R. (1971). Solid. St. Commun. 9, 519-22.

COWLEY, R.A. (1976). Phys. Rev. B13, 4877-4885.

COWLEY, R.A., AXE, J.D. and IIZUMI, M. (1976). Phys. Rev. Lett. 36, 806-809.

DE LANGE, R.J. and SMITH, E.L. (1975) in The Structure and Function of Chromatine, Ciba Found. Symp. 28, 59.

ELLIOTT, R.J., HARLEY, R.T., HAYES, W. and SMITH, S.R.P. (1972). Proc. R. Soc. Lond. A328, 217-266.

ENGELMAN, D.M., MOORE, P.B. and SCHOENBORN, B.P. (1976). Brookhaven Symp. on Neutron Scattering in Biology, IV20-IV37.

FATUZZO, E. and MERZ, W.J. (1967). Ferroelectricity (North-Holland Publ. Company, Amsterdam) 105-147.

GEHRING, G.A. and GEHRING, K.A. (1975). Rep. Prog. Phys. 38, 1-90.

GEHRING, G.A., MALOZEMOFF, A.P., STRANDE, W. and TYTE, R.N. (1972). J. Phys. Chem. Solids 33, 1499-1510.

GRIFFIN, J.A., LISTER, J.D. and LINZ, A. (1977). Phys. Rev. Lett. 38, 251-254.

GUINIER, A. and FOURNET, G. (1955). Small Angle Scattering of X-rays, (Wiley, New York).

HANSEN, P.E., JOHANSSON, T. and NEVALD, R. (1975). Phys. Rev. B12, 5315-5324.

HARLEY, R.T. (1977). Electron-Phonon Interactions and Phase Transitions (Plenum Press, New York) 277-296.

HARLEY, R.T. and MACFARLANE, R.M. (1975). J. Phys. C.: Solid St. Phys. 8, L451-L455.

HJELM, R.P., KNEALE, G.G., SUAU, P., BALDWIN, J.P., BRADBURY, E.M. and IBEL, K. (1977). Cell 10, 139-151.

HOLMES, L.M., ALS-NIELSEN, J. and GUGGENHEIM, H.J. (1971). Phys. Rev. B12, 180-190.

HOLMES, L.M., JOHANSSON, T. and GUGGENHEIM, H.J. (1973). Solid State Commun. 12, 993-997.

HOPPE, W., MAY, R., STÖCKEL, P., LORENZ, S., ERDMANN, V.A., WITTMANN, H.G., CRESPI, H.L., KATZ, J.J. and IBEL, K. (1976). Brookhaven Symp. on Neutron Scattering in Biology, IV38-IV98.

HUTCHINGS, M.T., SCHERM, R. and SMITH, S.R.P. (1975) AIP Conf. Proc. No. 29, 372-78.

JACROT, B. (1976). Rep. Progr. Phys. 39, 911-953.

JOEL, K. (1976). Master Thesis, unpublished.

KANDANROVE, G.S. and BEKETOV, V.N. (1974). Fiz. Tverd. Tela. 16, 1857-1862.

KITTEL, C. (1949). Rev. Mod. Phys. 21, 541-583.

KJEMS, J.K., (1977). Electron-Phonon Interactions and Phase Transitions (Plenum Press, New York). 302-322.

LARKIN, A.I. and KHMEL'NITZKII, D.E. (1969). Zh. Eksp. Teor. Fiz. 56, 2087-2098.

MØLLENBACH, K. (1975). Master Thesis, unpublished.

MØLLENBACH, K., KJEMS, J.K. and SMITH, S.H. (1977). Electron-Phonon Interactions and Phase Transitions (Plenum Press, New York) 323-326.

NORWELL, J.C. and SCHOENBORN, B.P. (1976). Brookhaven Symp. on Neutron Scattering in Biology, II12-II23.

SANDERCOCK, J.R., PALMER, S.B., ELLIOTT, R.J., HAYES, W., SMITH, S.R.P. and YOUNG, A.P. (1972). J. Phys. C.: Solid St. Phys. 5, 3126-3146.

SCHMATZ, W., SPRINGER, T., SCHELTEN, J. and IBEL, K. (1974). J. Appl. Cryst. 7, 96-116.

SCHNEIDER, J. (1974a) ibid, 7, 541-546.

SCHNEIDER, J. (1974b) ibid, 7, 547-554.

STUHRMANN, H.B. (1976). Brookhaven Symp. on Neutron Scattering in Biology, IV3-IV20.

STUHRMANN, H.B. and FUESS, H. (1976). Acta Cryst. A32, 67-74.

WELLS, M.R. and WORSWICK, R.D. (1972). Phys. Lett. A42, 269-71.

YEAGER, M.J. (1976). Brookhaven Symp. on Neutron Scattering in Biology, II13-II36.

APPENDIX A

Some important ellipse formulas

In calculating the resolution function it is important to describe an ellipse by conjungate diameters and to change description from one set of conjungate diameters to another. Here the few simple equations neccessary for these operations are given.

In a cartesian coordinate system with axis x and y the usual ellipse formula is

$$ax^2 + by^2 + cxy = 1$$

Let $\bar{X}_1$ and $\bar{X}_2$ be a set of conjungate diameters and let the components of the diameters along the coordinate axis be denoted with subscripts x or y.

Then

$$a = \frac{W_x^2}{|\bar{X}_1 \times \bar{X}_2|^2}, \quad b = \frac{W_y^2}{|\bar{X}_1 \times \bar{X}_2|^2} \quad \text{and} \quad c = \frac{-2W_{xy}}{|\bar{X}_1 \times \bar{X}_2|^2}$$

where

$$W_x^2 = X_{1x}^2 + X_{2x}^2$$

$$W_y^2 = X_{1y}^2 + X_{2y}^2$$

and

$$W_{xy} = X_{1x}X_{1y} + X_{2x}X_{2y}$$

In other words: if $\bar{X}_1$ and $\bar{X}_2$ are given then a, b and c can be calculated.

If a, b and c are given then a set of conjugate diameters $\bar{Y}_1$, $\bar{Y}_2$ can be calculated - provided one of the four coordinates of $\bar{Y}_1$ and $\bar{Y}_2$ is given as well. Suppose $Y_{1x} = 0$ then it is easy to find

$$Y_{1y}^2 = \frac{1}{a}$$

$$Y_{2x}^2 = (b - \frac{c^2}{4a})^{-1}$$

$$Y_{2y} = - \frac{c}{2a} \cdot Y_{2x}$$

APPENDIX B

Power expansion of the Helmholz energy in chapter 4

The calculation of equations (4.20) and (4.21) from equation (4.14) is lengthy but straightforward. Here are given some of the details.

Eq. (4.14) is

$$A = A_o - \tfrac{1}{2} \frac{1}{V_o} [illegible] - \frac{1}{V_o} [illegible] \cdot e + \tfrac{1}{2} ce^2$$

$$+ \frac{k_B T}{V_o} \frac{W}{(1+\Delta)} \tanh^{-1} (\frac{W}{(1+\Delta)}) + \tfrac{1}{2} \frac{k_B T}{V_o} \ln(1 - (\frac{W}{(1+\Delta)})^2)$$

Using (4.15) and (4.16) it is rewritten as

$$A = A_o - \tfrac{1}{2} \frac{1}{V_o} (1+\Delta) [illegible]$$

$$+ \frac{k_B T}{V_o} \frac{W}{(1+\Delta)} \tanh^{-1} (\frac{W}{(1+\Delta)}) + \tfrac{1}{2} \frac{k_B T}{V_o} \ln(1 - (\frac{W}{(1+\Delta)})^2).$$

With $x = \frac{W}{(1+\Delta)}$ it is found that

$$A = A_o - \tfrac{1}{2}\frac{1}{V_o}(\lambda+\mu) < \sigma^z >^2 + \frac{k_B T}{V_o}\left\{-\frac{1}{2}x^2 - \frac{1}{4}x^2 - \frac{1}{6}x^6 \ldots + x^2 + \frac{x^4}{3} + \frac{x^6}{5} + \ldots\right\}$$

Since $x = \left\{ < \sigma^z >^2 + \frac{\cdot^2}{(\lambda-\mu)^2} \right\}^{\frac{1}{2}} = \left\{ < \sigma^z >^2 + y^2 \right\}^{\frac{1}{2}}$

the second, fourth and sixth order term in $< \sigma^z >^2$ can be calculated.

The second order term

Second order terms from the expansion.

$$\frac{1}{2} + \frac{1}{3\cdot 4} \cdot 2y^2 + \frac{1}{5\cdot 6}\, 3y^2 + \ldots. =$$

$$\sum_{o}^{\infty} \frac{1}{(2n+1)\cdot 2}\, y^{2n}$$

$$= \frac{1}{2y} \tanh^{-1} y$$

Then the total second order term is

$$-\frac{1}{2}\frac{1}{V_o}(\lambda+\mu) + \frac{1}{2}\frac{k_B T}{V_o}\frac{\tanh^{-1} y}{y}$$

It must be a temperature dependent function f(T) that can be expanded close to T_D as

$$f(T) = f(T_D) + f'(T_D) \cdot (T - T_D)$$

The Landau ansatz says

$$f(T_D) = 0 = k_B T_D \frac{\tanh^{-1} y}{y} - (\lambda+\mu)$$

and it is seen that

$$\frac{df(T)}{dT} = \frac{k_B}{V_o} \frac{1}{2} \frac{\tanh^{-1} y}{y}$$

Thus the second order term is

$$\frac{k_B}{V_o} \frac{1}{2} \frac{\tanh^{-1} y}{y} (T-T_D) < \sigma^z >^2$$

Using (4.19) it can be rewritten in terms of the order parameter as

$$\frac{k_B}{V_o} \frac{1}{2} \frac{\tanh^{-1} y}{y} (1-y^2) \cdot (T-T_D) \cdot Q^2$$

or

$$a = \frac{1}{2} \frac{\tanh^{-1} y}{y} (1-y^2).$$

The fourth order term

Fourth order terms from the expansion

$$\frac{1}{3 \cdot 4} + \frac{3}{5 \cdot 6} \cdot y^2 + \frac{6}{7 \cdot 8} \cdot y^4 + ... =$$

$$\sum_1^\infty \frac{1}{4} \frac{n}{(2n+1)} y^{2n-2} =$$

$$\frac{1}{8} \left\{ \sum_{n=1}^{\infty} y^{2n-2} - \sum_{n=1}^{\infty} \frac{1}{2n+1} y^{2n-2} \right\} =$$

$$\frac{1}{8} \left\{ \sum_{n=o}^{\infty} y^2 - \frac{1}{y^3} \sum_{n=o}^{\infty} \frac{1}{2n+1} y^{2n-2} + \frac{1}{y^2} \right\} =$$

$$\frac{1}{8} \left\{ \frac{1}{1-y^2} - \frac{\tanh^{-1} y}{y^3} + \frac{1}{y^2} \right\}$$

Thus the fourth order term is, using (4.19) again:

$$\frac{k_B}{V_o} T \frac{1}{8} \left\{ \frac{1}{1-y^2} - \frac{\tanh^{-1} y}{y^3} + \frac{1}{y^2} \right\} (1 - y^2)^2 \cdot Q^4$$

or

$$b = T \frac{1}{8} \left\{ \frac{1}{1-y^2} - \frac{\tanh^{-1} y}{y^3} + \frac{1}{y^2} \right\} (1 - y^2)^2$$

The sixth order term

Sixth order terms from the expansion

$$\frac{1}{5 \cdot 6} + \frac{4}{7 \cdot 8} \cdot y^2 + \frac{10}{9 \cdot 10} \cdot y^4 + \ldots\ldots =$$

$$\frac{1}{12} \sum_{n=1}^{\infty} \frac{n(n+1)}{(2n+3)} y^{2n-2}$$

$$\frac{1}{24} \left\{ \sum_{1}^{\infty} (n-1) y^{2n-2} + \sum_{1}^{\infty} \frac{n+3}{2n+3} y^{2n-2} \right\} =$$

$$\frac{1}{48} \left\{ \sum_{1}^{\infty} (2n-2) y^{2n-2} + \sum_{1}^{\infty} y^{2n-2} + 3 \sum_{1}^{\infty} \frac{1}{2n+3} y^{2n-2} \right\} =$$

$$\frac{1}{48} \left\{ 2 \frac{y^2}{(1-y^2)^2} + \frac{1}{(1-y^2)} + \frac{3}{y^5} \left(\tanh^{-1} y - y - \frac{y^3}{3} \right) \right\} .$$

Thus the sixth order term is, using (4.19) once more:

$$\frac{k_B}{V_o} T \cdot \frac{1}{48} \left\{ 2 \frac{y^2}{(1-y^2)^2} + \frac{1}{1-y^2} + \frac{3}{y^5} \left(\tanh^{-1} y - y - \frac{y^3}{3} \right) \right\}$$

$$\cdot (1-y^2)^3 \cdot Q^6$$

or

$$C = T\frac{1}{48}\left\{2\frac{y^2}{(1-y^2)^2} + \frac{1}{1-y^2} + \frac{3}{y^5}\left(\tanh^{-1}y - y - \frac{y^3}{3}\right)\right\}\left(1-y^2\right)^3$$

APPENDIX C

A model for domain diffraction

Diffraction from a one-dimensional domain structure

Consider first a one-dimensional domain structure where the widths of the domains are given by a stokastic function by the following rule. The probability of having a domain wall between positions x and x + dx is

$$ds = \kappa \cdot dx$$

From this assumption it follows that the probability of having exactly n domain-walls within the distance x is

$$P_n(x) = \frac{(\kappa \cdot x)^n}{n!} e^{-\kappa \cdot x}$$

and the average domain width is κ^{-1}.

The domain-domain correlation function is then

$$G(x) = e^{-2\kappa \cdot x} \cdot M(T)^2$$

and its Fourier-transform

$$S(q) = \frac{2\kappa}{(2\kappa)^2+q^2} \cdot M(T)^2$$

where M(T) is magnetization density.

A finite domain-wall width will enter the calculations by a function multiplied on S(q). This function can be viewed as a formfactor since the neutron scattering cross-section is given by

$$\frac{d\sigma}{d\Omega} \propto \left(\frac{M(T)}{M_o}\right)^2 \cdot \frac{2\kappa}{(2\kappa)^2+q^2} \cdot f(q)$$

Domain diffraction in three dimensions.

Consider a three-dimensional model which is a simple isotropic extension of the one-dimensional model discussed in the preceding section.

Now the domain-domain correlation function is

$$G(r) = e^{-2\kappa \cdot r} \cdot M(T)^2$$

and its fourier transform

$$S(q) = \int_0^{\pi} \int_0^{\infty} r^2 \sin\theta \, dr \, d\theta \, G(r) \, e^{-iq \cdot r \cdot \cos\theta}$$

$$\propto M(T)^2 \frac{2\kappa}{((2\kappa)^2 + q^2)^2}$$

Domain diffraction in $LiTbF_4$

Consider a domain model which is isotropic in the x-y plane with an average domain width κ^{-1} but where the domain width along the Z-axis is c/κ.

This structure is mapped onto another space by

$$\begin{pmatrix} x \\ y \\ z \end{pmatrix} \rightarrow \begin{pmatrix} x' \\ y' \\ z' \end{pmatrix} = \begin{pmatrix} x \\ y \\ z/c \end{pmatrix}$$

In the new space the structure is isotropic i.e. the structure calculated in preceding section. The cross-section in the original space is found by transforming the isotropic cross-section by

$$\begin{pmatrix} q'_x \\ q'_y \\ q'_z \end{pmatrix} \rightarrow \begin{pmatrix} q_x \\ q_y \\ q_z \end{pmatrix} = \begin{pmatrix} q'_x \\ q'_y \\ q'_z \cdot c \end{pmatrix}$$

and

$$S(q) = M(T)^2 \frac{\kappa^2}{((2\kappa)^2 + q_x^2 + q_y^2 + c^2 q_z^2)^2}$$

This result assumes infinitely thin domain walls. Finite domain walls can be accounted for in the way as shown in the discussion of the one dimensional model.

Sales distributors:
Jul. Gjellerup, Sølvgade 87,
DK-1307 Copenhagen K, Denmark

Available on exchange from:
Risø Library, Risø National Laboratory,
P. O. Box 49, DK-4000 Roskilde, Denmark

ISBN 87-550-0580-2
ISSN 0106-2840